

**A HIGH-RESOLUTION MODELING STUDY OF CONVECTIVE INITIATION  
ON 19 JUNE 2002 DURING IHOP**Qi-Wei Wang<sup>1</sup> and Ming Xue<sup>\*1,2</sup>Center for Analysis and Prediction of Storms<sup>1</sup> and School of Meteorology<sup>2</sup>  
University of Oklahoma, Norman Oklahoma 73072**1. INTRODUCTION**

Accurate prediction of warm-season convective rainfall has remained a challenging problem in the United States. At present, the quantitative precipitation forecasting (QPF) skill associated with these warm-season systems is still very low (Fritsch and Carbone 2004). It is an essential step to improve the QPF skill by improving the knowledge of the timing, location and intensity of convective initiation (hereafter, CI) (Weckwerth et al. 2004; Weckwerth and Parsons 2006). While the prediction of CI is partly related to the accurate representation of important smaller-scale physical processes in mesoscale numerical models, and can also be highly dependent on very accurate estimates of water vapor within the boundary layer (Crook 1996; Weckwerth et al. 2004). It is because the water vapor is in high temporal and spatial variability within the boundary layer, and can evidently influence the vertical profile of buoyancy, which the CI sensitively dependent on. To understand the CI processes and QPF questions using more accurate observations of water vapor, the International H<sub>2</sub>O Project (IHOP\_2002; Weckwerth et al. 2004) field experiment was carried out in the spring of 2002.

Wilson and Roberts (2006) systematically summarized all the CI events and their evolution during the IHOP period based on observational data, among which there were several representative CI cases. The 24 May 2002 dryline CI case was numerically studied in detail by Xue and Martin (2006a,b, hereafter XM06a and XM06b, respectively). Liu and Xue (2008, hereafter LX08) numerically simulated and investigated the 12 June 2002 CI case and its storm evolution.

In the case study of XM06a,b, the Advanced Regional Prediction System (ARPS; Xue et al. 2000, 2001, 2003) and its data assimilation system were employed to simulate the events at 3- and 1-km horizontal resolutions. The CI did not occur at the intersection point between the dryline and a southwest-northeast-oriented surface cold front located in the north, or at the dryline-cold front "triple point", the true CI that actually occurred farther south along the dryline. Accurate timing and location of the initiation of three initial convective cells along the dryline are captured in the model at the 1-km resolution. A conceptual model proposed in

XM06b summarized that the interaction of the finescale boundary layer horizontal convective rolls (HCRs) with the mesoscale convergence zone along the dryline was responsible for determining the exact locations of convective initiation. Using a similar approach as XM06a,b, LX08 studied the CI processes and subsequent storm evolutions in the 12 June 2002 case. This case also involved a dryline intersecting a cold front, but with a further complex situation that a cold pool and the associated outflow boundary ran roughly east-west and intercepted both cold front and dryline near its west end. Their experiment simulations captured the initiation of four groups of convective cells rather well, and a secondary initiation of cells due to the collision between the main outflow boundary and the gust fronts developing out of model-predicted convection earlier was also captured accurately about 7 h into the prediction.

Another typical CI case involving a dryline intersecting a cold front was on 19 June 2002 during IHOP. This case took place near the northwest of the IHOP study area and included three distinct CIs, one started in the front-dryline transition zone over southeast Colorado and moved northeast quickly following the dry air extrusion between the cold front and the dryline, the second developed along the quasi-stationary dryline near Goodland, Kansas, and the third located further north over the cold front near Frontier, Nebraska. For the second CI, an airborne Doppler radar as well as a number of other mobile research platforms converged on the dryline before and during the initiation of deep convection, and the evolution and finescale structure of the dryline that initiated a line of thunderstorms had been analyzed by Murphey et al. (2006) in detail.

The boundary intersections, such as the dryline-cold front "triple point" and the outflow boundary-dryline intersection, are conventionally highlighted as the location of highest CI potential. But the most observation instruments deployed near the triple point in 24 May 2002 case missed the true CI that actually initiated along the dryline. The 12 June 2002 case was also a "convective initiation failure" in a region near the intersection point of the outflow boundary and dryline which was chosen for intensive observations (Markowski et al. 2006). For this case, the CIs were not initiated at the triple point either. Clearly, further examining and better understanding of the CI mechanisms in this and more cases are needed.

---

\* Corresponding author address: Dr. Ming Xue, Center for Analysis and Prediction of Storms, University of Oklahoma, 120 David L. Boren Blvd, Norman OK 73072. Email: mxue@ou.edu.

In this study, a similar approach as that in XM06a,b and LX08 is used to study the CI processes in the 19 June 2002 case. As in XM06a,b and LX08, 3- and 1-km

horizontal resolution grids are used in this study (Fig. 1), and additional numerical experiments are conducted to evaluate the impact of various data assimilation configurations. The results of this study will be presented in three parts. In this first part (Part I), an overview of the case is presented, together with a brief description of the numerical model and its configurations, and of the data assimilation method and observation data used. This part will focus on the mesoscale environment of the CIs. In the second part of this paper (hereafter Part II), a detailed analysis of the results of the 1-km grid will be presented, with the primary goal of understanding the exact processes responsible for the CIs. The first two parts will mainly analyze the results of the control data assimilation experiment. In the third part of this paper, the impact of a number of data assimilation configurations on the prediction of CIs will be further examined through a set of sensitivity experiments as an ensemble approach.

The rest of this paper is organized as follows. In section 2, we discuss the synoptic and mesoscale environment of the 19 June 2002 case, the cold front-dryline interaction and the evolution of the boundaries, and the subsequent evolution of the CI cells and their eventual organization into deep convection. Section 3 introduces the numerical model used and its configurations, as well as the design of sensitivity experiments. The results are presented and discussed in sections 4 and 5 and a summary is given in section 6.

## 2. OVERVIEW OF THE 19 JUNE CASE

At 1800 UTC (hereafter, all times are UTC) 19 June 2002, a shallow trough was situated over northwest Wyoming and a high was located in southern Kansas and northern Oklahoma on the 250-hPa (Fig. 2a). There was a broad region of strong southwest winds between the trough and the high with a jet maximum over  $55 \text{ m s}^{-1}$  located to the east of the trough. At the 500-hPa level (Fig. 2b), a trough extended from northern Wyoming to eastern Montana with a jet maximum over  $35 \text{ m s}^{-1}$  to its right and a high was over the southwest of Kansas. The weather pattern on the 250-hPa is similar to that on the 500-hPa, the three CIs of the 19 June 2002 case initiated approximately to the northwest side of the high, while the trough is located faraway to the northwest of the CIs. A short trough is found to the southwest of the high both on the 250-hPa and 500-hPa, which is favorable for the first CI over southeastern Colorado. A small south wind maximum center over  $15 \text{ m s}^{-1}$  is also found near the northwest side of the high on the 250-hPa, and this secondary jet is favorable for the second CI over northeastern Kansas due to jet-induced ageostrophic circulation. A strong west-southwesterly flow exceeding  $20 \text{ m s}^{-1}$  between the high to its southeast and a trough to its northwest was over the northeastern Nebraska and southeastern South Dakota at the 700-hPa level (Fig. 2c), and over northeastern Kansas, Southeast Nebraska and southwest Iowa on the 850-hPa (Fig. 2d). This flow brought moist air from the Gulf into the region east of the dryline and the cold

front (Fig. 2c, d and Fig. 3a). A closed circulation center is found in the central South Dakota on the 850-hPa, which is also seen at the surface (Fig. 3a). Behind the cold front is the shallow cold air that moved along the flank of Colorado Rocky mountains pushing the cold front southeastward, toward the dryline (Fig. 3a). At 1800 UTC, the triple point was located near the center of Colorado-Kansas board (Fig. 3a). As the cold front advanced, the triple point shifted northeastward. In the next few hours, the dry air between the cold front and the dryline was evidently extruded and pushed toward northeast following the triple point.

Figure 3b shows the convective available potential energy (CAPE) and convective inhibition (CIN) maps at 1800. Large CAPE regions are seen near and/or to the east of the cold front and the dryline. A local CAPE maximum over  $3500 \text{ J kg}^{-1}$  (denoted by H) is found before the cold front at the southwest corner of Nebraska, where there are less CIN. This maximum is believed to be responsible for the third CI of this study. Another CAPE maximum near the triple point is found farther south before the dryline over the Oklahoma panhandle. Between the two maximum is a transition zone of less CIN and relative large CAPE with a larger CIN region (denoted by  $H$ ) to the east. The first and the second CI of this study initiated near this zone during the triple point migrated northeastward.

Figure 4 shows the Geostationary Operational Environmental Satellite (GOES) visible images taken at 1945, 2015, 2045, 2115, 2145 and 2215 on 19 June 2002. At all these times, a region southeast of Colorado is covered by cumulus humilis clouds, while another region south of Kansas is covered by altostratus fractus clouds. The cumulus humilis clouds southeast of Colorado are believed to be related to local boundary-layer eddy and roll activities, and the altostratus fractus clouds south of Kansas to be related to high-level uplift along the cold front. At 1945, the shallow clouds southeast of Colorado show a tendency of intensifying along its northeast side (as indicated by white arrows in Fig. 4a), and one identifiable large cumulus cloud A (hereafter, CI-A) is seen there by 2015 (Fig. 4b). This cloud is also seen in the radar observations at 2000 (Fig. 5a) though the radar echo is still weak. By 2045 (Fig. 4c), CI-A continually developed, and at the same time, a line of convective cells appear over the northwestern Kansas, to the northeast of CI-A. At 2115 (Fig. 4d), CI-A got further developed, and the convective line became more clear, extending from the middle of Kansas east border to southwest Nebraska. By 2145 (Fig. 4e), CI-A became fully developed and merged with the southwest part of the growing convective line, two convective cloud cluster B and C (hereafter, CI-B and CI-C) got quick initiation at this time from the shallow cloud signals denoted by arrows in Fig. 4d. By 2215 (Fig. 4f), the compact anvils of CI-A shown the weakening of this convective cluster, while CI-B and CI-C got strong development. All the three convective clouds can be seen in the radar observations at 2200 (Fig. 5c). It is

clear that CI-A started close to 2015 and CI-B and CI-C initiated near 2145.

### 3. NUMERICAL MODEL, DATA AND EXPERIMENT DESIGN

Version 5 of ARPS is used in this study. The ARPS is a general-purpose nonhydrostatic model suitable for mesoscale and convective-scale simulation and prediction. A  $1003 \times 1003$  model grid domain at 1-km horizontal resolution nested inside a 3-km  $803 \times 603$  grid domain is used (Fig. 1). In the vertical, a 53 stretching layer is formulated in a generalized terrain-following coordinate, with the grid spacing increases from about 20 m near the ground to about 800 m near the model top that is located about 20 km above sea level. The model terrain and land surface characteristics on the 3- and 1-km grids are created in the same way as in XM06a,b and LX08. The lateral boundary conditions (LBCs) for the 3-km grid are from time interpolations of 6-hourly National Centers for Environmental Prediction (NCEP) Eta Model analyses and the 3-h forecasts between the analyses, while the 1-km grid gets its LBCs from the 3-km forecasts at 10-min intervals.

The ARPS is used in its full physics mode (see Xue et al. 2000, 2001). The microphysics scheme is the Lin et al. (1983) three-ice microphysics. The 1.5-order (turbulent kinetic energy) TKE-based subgrid-scale turbulence parameterization and TKE-based PBL-mixing parameterization (Sun and Chang 1986; Xue et al. 1996) are used. Also used is the National Aeronautics and Space Administration (NASA) Goddard Space Flight Center (GSFC) long- and shortwave radiation package (Chou 1990, 1992; Chou and Suarez 1994), and the land surface condition is predicted by a two-layer soil-vegetation model initialized using the state variables presented in the Eta analysis.

The initial conditions of our simulations are created using the ARPS three-dimensional variational data assimilation system (ARPS3DVAR; Gao et al. 2002). The cold-start mode where the analysis is performed only once using an Eta analysis as the background is configured as the control data assimilation experiment, also designed are a set of sensitivity experiments with different intermittent assimilation cycles where the cycled analyses using ARPS forecasts from the previous forecast cycles as the background. For all experiments to be presented, the initial conditions, created with or without assimilation cycles, are valid at 1800 UTC 19 June. In addition to routine and special conventional observations, various remote sensing instruments were deployed on this day (Weckwerth et al. 2004). As in LX08, conventional forms of data are assimilated into the model initial condition, including those of (regular and mesonet) surface stations, upper-air soundings, and wind profilers. Available aircraft data [i.e., the Meteorological Data Collection and Reporting System (MDCRS)] are also included. Table 1 lists the

standard and special datasets used, together with their key characteristics. The data sources are similar to that used in LX08, except that more 11-station ARM surface data are added and the RAOB data at 1500 are missing. Figure 1 marks most of the observation sites used in this study, and data from six of the Weather Surveillance Radar-1988 Doppler (WSR-88D) radars in the region are used extensively for verification. Table 2 gives the observations analyzed and the horizontal and vertical influence radius for each analysis pass used in ARPS3DVAR. Grid points are chosen in ARPS3DVAR as the vertical influence radius instead of kilometer in ARPS Data Analysis System (ADAS; Brewster 1996) which was used in XM06a,b and LX08. The vertical influence scales in this study are generally smaller at lower levels but larger at higher levels than the corresponding ones used in XM06a,b and LX08, due to the vertically-stretching coordinate.

After an initial condition is obtained at 1800 UTC on the 3-km grid, the ARPS model is integrated for 18 hour until 1200 UTC 20 June 2002, the first 9 hour covers the full evolution of the three CIs. The 1-km grid forecast also starts at 1800 UTC, with the initial condition interpolated from the 3-km grid, and runs until the same ending time. The gridded output interval is 10-min for the 3-km run and 1-min for the 1-km run, and results from the 1-km grid will mainly be analyzed with the help of various animations. As pointed out earlier, we will present only the results from the control data assimilation experiment in this part (Part I) with focus on the mesoscale environment of the CIs. Detailed analyses on the convective initiation mechanisms will be presented in Part II, and sensitivity of the CIs to the data assimilation configurations will be further discussed in Part III.

### 4. RESULTS AND DISCUSSIONS

#### 4.1 *The forecast of convective storms and the general evolution of three focused CIs*

##### 1) The forecast of convective storms

In Fig. 5, the model-predicted composite reflectivity, dBZ, is compared against the corresponding radar observations at 2000, 2100, 2200, and 2300 on 19 June 2002. Here the model reflectivity is derived using the formula defined in Tong and Xue (2005) from predicted hydrometeors, including rainwater, snow, and hail mixing ratios. The radar composite reflectivity is defined as the maximum reflectivity in the vertical column, and obtained from six radars marked as filled-triangles in Fig.1 using the Warning Decision Support System (WDSS-II; Lakshmanan et al. 2007). The three regions where CI-A, B, and C initiate and subsequently develop into the three convective storms are framed in Fig. 5 as three small boxes over southeast Colorado, northeast Kansas, and south-central Nebraska respectively.

At 2000, the radar observations show convection A over the southeast corner of Colorado (Fig. 5i). In the model, similar storms are seen at this time both on the 3-km (Fig. 5a) and 1-km forecast (Fig. 5e). By 2100, the convection A exhibited several centers of intense dBZ on the observations (Fig. 5e), with new convective cell developing at the northeast of this convective cluster (Fig. 5i and Fig. 5j). The 3-km forecast (Fig. 5b) captured the multi-cell structure of convection A, but missed the new developing cell northeast which was predicted in the 1-km forecast (Fig. 5f) and seen on the observation (Fig. 5j). At this time, a line of thin reflectivity appears to the northeast of convection A which whereafter grew into a convective line along the dryline in Fig. 4d.

By 2200, the thin convective line demonstrates further development joining with convection A, and convection B and C have initiated and risen up as isolated convective storms (Fig. 5k). The 3-km forecast at this time (Fig. 5c) missed both the development of the convective line and the convection B, while the 1-km simulation gave a well prediction of convection B with a later and weaker forecast of the convective line to its southwest. The convection C was predicted with further delay and did not present in the model forecast at 2200.

By 2300 (Fig. 5l), the convection B and C and the convective cells between them got evident development. The convection zone from convection A to C nearly located where they were at 2200, which denoted that the cold front and the dryline were quasi-stationary during this time. In the 3-km forecast (Fig. 5d), the convection zone northeast to convection A almost initiated at the same time as isolated convective cells. The simulation at this resolution can't resolve the smaller convective structures which are comparable to the observations. In the 1-km forecast (Fig. 5h), the convection C was predicted over south-central Kansas with weaker intensity due to a later initiation time. The convection B and the convective line joining with convection A were forecasted with excessive intensity, while the convection A still extended from southeastern Colorado to the northeast which were in good agreement with the observations. At all four times, the storms over the joint area of Wyoming, Colorado and Nebraska are also captured in the 3-km and 1-km forecasts, while the scattered weak radar echoes over Colorado were exaggeratedly predicted due to the intricately-disturbed boundary layer over mountainous region or the transition zone between cold front and the dryline.

## 2) Evolution of CI-A

The small box over southeast Colorado in Fig. 5e and Fig. 5i where CI-A initiated is enlarged in Fig. 6. The CI focused over this region which subsequently gets further development locates near the joint area of county Bent, Prowers and Baca (Fig. 6a-d). At 1930, observed reflectivity echoes dispersedly exhibited for the first time over and to northwestern Baca county where four cells

were identified (Fig. 6a). During the next 30 minutes, all the four cells moved to the northeast and got evident development with cell 1 growing fastest merging with cell 2 (Fig. 6b). By 2030 (Fig. 6c), the rapider-moving cell 3 caught up with cell 2 and made the merging cell a quick enhancement up to 45 dBZ with larger extension. The cell 4 ahead of the merging cell also developed into stronger reflectivity echoes greater than 40 dBZ during the last hour. By 2100 (Fig. 6d), all the cells tended to organize as a convective zone, with cell 1 and cell 4 being linked by growing echos between them and two new cells tailing after cell 3. In the next 3 hours, the observations show that the southwest end of the convective zone is almost steadily located over the northwest corner of Baca county (Fig. 5k-l), which indicates that there is an incessant local condition favoring for CI there.

After closely examining the simulated storm evolution over CI-A region, the model time the same as the observations is chosen to make the comparison. The cells comparable with that in the observations are marked as the same number. At 1930 (Fig. 6e), cell 1, 2 and 4 had not appeared yet and only cell 3 could be identified. The original reflectivity echoes of cell 3 and the cells nearby first shown up over Las Animas county about 45 minutes earlier (not shown). As the storms over east-central Colorado (Fig. 5), these convective cells over Las Animas county were also over-predicted, which made cell 3 much stronger than the observations by 1930 UTC. By 2000 (Fig. 6f), cell 1 and 2 had arisen locally at southeast Bent county, while cell 3 moved northeastward across the Las Animas-Baca border and linked with cell 1 and 2. New echo center formed in the left-forward of cell 3 (denoted by the arrow 3 in Fig. 6f) during the next 30 minutes, and at the same time the left- and right-side echo centers of cell 3 weakened away while the tail echo center strengthened. The new echo center gradually merged together with the quickly-developing cell 1 and 2, this made a strong joint cell comparable with the observations at 2030 (Fig. 6g). A new cell to the northeast of the joint cell also shown up by 2030, which was believed to correspond to the observational cell 4. By 2100 (Fig. 6h), the simulations shown that cell 4 had blended with the joint cell resembling the linkage of them in the observations. The structure of new cell tailing from the joint cell in Fig. 6d was also seen in Fig. 6h as reflectivity echoes greater than 50 dBZ attaching to the simulated joint cell. The southwest-northeast convective zone would soon establish when the joint cells combined with the new cells formed to its northeast. Note that inercacious convective cells moving eastward from the over-predicted region are all the way simulated to the west of this CI, which slightly changes the shape of the credibly-simulated reflectivity echoes.

In fact, the representative of CI-A, cell 1, locally initiated at 1950 UTC with the 10 dBZ reflectivity echo first showing up (Fig. 10a). Detailed comparison with Fig. 6a shows that the simulated CI-A is about 5 km west to the observations with 20 minutes delay.

### 3) Evolution of CI-B

Fig. 7 demonstrates the CI-B by enlarging the small box over northwest Kansas in Fig. 5f and Fig. 5j. At 2110 (Fig. 7a), observed reflectivity echoes of CI-B greater than 20 dBZ presented for the first time over Logan county, Kansas. Twenty minutes later (Fig. 7b), it moved across the Logan-Thomas border along the dryline and less changed its intensity. While in the next 30 minutes, this convective cell got a jump development, quickly moved to the east Thomas-Rawlins border with its intensity increasing from 20 dBZ to 45 dBZ (Fig. 7c). By 2230 (Fig. 7d), the convection B continuously strengthened and subsequently joined with the rapidly-rising convective cells to its northeast. During this period, the convective line to the southwest of CI-B also exhibited a gradual growing.

The simulated CI-B is about 30 minutes later than the observations (Fig. 7e-f), with the 10-20 dBZ reflectivity echo first showed up at 2138 (Fig. 10b). At 2140 (Fig. 7e), the original cells of convection B and the convective line both emerged, but not joined together as the observations. The cell B was located over northwest Sheridan county at this time, about 80 km northeast to the observational cell B at 2110. During the next 2 hours (Fig. 7f-h), the convection B got further development with multi cells embedded in. The storms in this region are exaggeratedly predicted with larger intensity and spread, while the CI-B and the convective line can be fairly compared with the observations.

### 4) Evolution of CI-C

The evolution of CI-C is illustrated in Fig. 8 within the enlarged box over south-central Nebraska in Fig. 5g and Fig. 5k. The forecast of this CI is also about 30 minutes later than the observations. At 2140 (Fig. 8a), the observed initial convection was over Frontier county, Nebraska. In the next 80 minutes (Fig. 8c-d), this CI slightly moved toward the east border of Frontier county and showed a violent development uniting the rapidly-rising convective cells to its southwest. By 2300 (Fig. 8d), the maximum echo was over 70 dBZ locating at Red Willow-Frontier border, and the width of echo greater than 20 dBZ was even more than 100 km.

For the simulations, a lot of high level clouds were mis-resolved in the model at 2210 (Fig. 8e), the true CI labeled as C located in Gosper county at this time, about 60 km east to the observed CI (Fig. 8a). In the next 20 minutes, new convective cells initiated both southwest and northeast of the CI. All the cells slightly moved toward the northeast and gradually merged together. By 2230 (Fig. 8f), a short intense convective line formed over the joint area of Gosper, Phelps and Dawson county. Other convective cells along the cold front also emerged northeast and southwest of the convective line at this time. During the next hour, all the convections conjoined to a long convective line with the former short convective line developing into the most

intense storms (Fig. 8g-h). The simulated convection C is in good agreement with the observations in shape and intensity, except the location and the extension of echoes less than 30 dBZ.

In general, the control data assimilation experiment captured the three CIs and their evolution rather well. The first focused convection initiated ~20 min later than and ~5 km west to the observations. The CI-B and CI-C both started ~30 min later than the observations, with location errors near 80 and 60 km respectively.

#### 4.2 The evolution of cold front and dryline, the CIs and their mesoscale background

##### 1) The cold front, dryline and the initiation of convections

The model-predicted surface winds, water vapor mixing ratio ( $q_v$ ) at 1-km horizontal resolution are shown in Fig. 9. The surface cold front is outlined as thick-dashed line, and the zone of strong moisture gradient ( $10-11 \text{ g kg}^{-1}$ ) is shaded as dark green, which denotes the dryline before the cold front or dry air boundary after it. At the initial condition time (Fig. 9a), the zone of strong gradient has a width of about 20 km due to the coarse background directly interpolated from NCEP Eta model analysis. The dryline at this time is oriented roughly from the east of Kansas north border to northeast New Mexico, with the cold front locating after it from central Nebraska to southeast Colorado. The red squares A, B, and C mark the locations where CI-A, CI-B, and CI-C will first start.

At 1950 (Fig. 9b), the model-predicted dryline got much narrower and showed a rough structure. Over southeast Colorado, both the cold front and the dryline slightly shifted northwestward due to stronger low-level south flow, the air mass between the cold front and the dryline became much dryer at this time, and CI-A initiated just near the dryline along the southeast margin of the dryer air mass. Note that the cold front over south-central Nebraska approached toward southeast evidently by 1950 UTC, the north cold air mass behind the front distorted the dry air boundary into northeast Colorado, which shaped a dry tongue structure over northwest Kansas as described in Murphey et al. (2006).

By 2138 (Fig. 9c), the north and northeast winds behind the cold front had driven the dry air boundary into the northwest of Kansas, and at the same time, the dryline across Colorado-Kansas border was slightly pushed northward by the stronger south winds. The dry tongue became narrower and the dry air between the cold front and the dryline was further extruded. This made a slender eastward bulge of the dryline over northwest Kansas, which is consistent with the wavelike pattern of the dryline observed by the WSR-88D located at Goodland, Kansas (Murphey et al. 2006). At this time, the model-predicted CI-B initiated before the dryline and near the tip of the dry tongue. The initiation of

convection B will be further analyzed and compared with observations in vertical cross sections later.

Three major moisture bands with  $q_v$  greater than  $15 \text{ g kg}^{-1}$  can be found at 2138 UTC (Fig. 9c). One is over south Nebraska behind the cold front, the other two are north-southwardly oriented locating over Kansas. During the next 32 minutes, the cold front approached slightly southeastward, while the two moisture bands over Kansas moved and extended northward. By 2210 (Fig. 9d), the right moisture band over Kansas spreaded further north and conjoined with the moisture band behind the cold front near the point C, where CI-C came to its initiation.

## 2) Horizontal and vertical cross sections at CI time

Fig. 10 shows the near-surface ( $\sim 30 \text{ m AGL}$ ) moisture convergence fields for 1950, 2138, and 2210 UTC 2002, the times when 10-20 dBZ contours of composite reflectivity associated with CI-A, CI-B, and CI-C first appear. Also shown in the plots are the wind vectors and  $q_v$  at the same level. There exists significant small-scale variabilities in the  $q_v$  and wind fields within the CI regions, which are the results of boundary layer horizontal convective rolls (HCRs) or the less organized open boundary layer convective cells (OCCs) as mentioned in Xue and Martin (2006a, b).

Over the CI-A region, the earlier- and over-predicted convections over Las Animas county in Fig. 6e is originated from the exaggeratedly-simulated OCCs between the cold front and the dryline west to that county at a earlier time. The HCRs in CI-A region gradually well organized as time going on, a zone with large gradient of  $q_v$  could be seen locating northeast-southwesterly near the southeast edge of cell 3 by 1930 UTC (Fig. 6e). Corresponding to the gradient zone of  $q_v$ , a moisture convergence zone had clearly presented along the primary dryline convergence boundary (PDCB) by 1950 (Fig. 10a). Also seen at 1950 UTC are three more organized moisture convergence bands (MCBs) connecting with the moisture convergence zone, which are reorganized from the less organized MCBs before the dryline. The evolution of the moist convergence zone along the dryline shows that it is formed mainly by concentrating the MCBs southeast of the dryline which are driven by strong south flow, while the weaker MCBs between the cold front and the dryline also have a secondary contribution. The CI-A initiated slightly to the east of a MCB within the moisture convergence zone (Fig. 10a). The first cell of CI-A locally generated and clearly separated from the southwest storms at this time.

For the CI-B (Fig. 10b), the MCBs before the dryline are better-organized, which show more dense distribution and are about parallel to the PDCB. While the moisture convergence after the dryline and/or the cold front shows a disordered structure due to more irregular boundary layer heating. The parallel MCBs tend to merge together where they meet the irregular moisture

convergence curves near the PDCB. As a result of the merger of the MCBs, low-level convergence maximum will be rapidly enhanced. The CI-B was immediately initiated west of such an enhanced low-level convergence.

There are no obvious MCBs parallel each other in CI-C region (Fig. 10c). The irregular MCBs quickly gathered together near the cold front, where the low-level convergence rapidly strengthened. The CI-C initiated between two merging low-level MCBs just before the cold front. This situation is not like that of CI-A and CI-B which locate east and west of MCB respectively. The connection of these initial cells with the low-level convergence maximum will be analyzed in more detail in Part II of this case study.

In Figs. 11a-b, c-d, and e-f, the equivalent potential temperature ( $\theta_E$ , contours), vertical velocity (gray shading), wind fields (barbs), and the 10 dBZ reflectivity (bold solid contours) are shown in northwest-southeast cross sections through CI-A, CI-B, and CI-C, respectively. The low-level air masses consistently moving along the cross sections are outlined with thick-dashed lines. The thick 333 K  $\theta_E$  contours denote the boundary layer top.

At the initial condition time (Fig. 11a), two air masses intersected within the boundary layer along the cross section of CI-A with the northwest wind dominating and flowing over the southeast wind. The southeast air mass was confined in a more stable moist layer with a larger gradient of  $\theta_E$  at this time. Above the boundary layer, the northwest wind extended to about 5 km mean sea level (MSL), while between  $\sim 5 \text{ km MSL}$  and  $\sim 7 \text{ km MSL}$  is a layer with uniform southeast wind along the cross section. So there is initially a thick wind shear in the middle level in CI-A region. By the CI time (Fig. 11b), the middle-level wind shear had developed into a series of middle-level HCRs. Wave patterns of  $w$  can be seen throughout the plotting domain, which reflects roll and eddy activities at middle and lower levels and gravity wave activities above. The low-level HCRs behind the dryline are more active than that before the dryline. The enhanced updraft triggering the CI due to the interactions between the low-level HCRs and the middle level ones will be further analyzed in Part II. The more stable southeast wind within the boundary layer had moved slightly toward northwest and strengthened showing a strong upsurge where the CI-A initiated above. The upsurge region is corresponding to the PDCB in Fig. 10a, within which is the well-mixed neutrally stable and moist layer as shown in Fig. 14d.

The initial condition along the cross section of CI-B (Fig. 11c) was evidently different with that of CI-A. The low-level southeast air mass initially dominated, while was as stable as the northwest air flow. The  $\theta_E$  contours had a broad horizontal distribution within the low-level. There was not a middle level wind shear as that of CI-A either. The northwest wind stretched up to  $\sim 8 \text{ km}$  to the

northeast of this section, and gradually descended to ~6 km to the southeast of the section. By the CI time (Fig. 11d), no middle level HCRs formed, the  $w$  fields showed that rolls and eddies were confined within but transmitted penetrating the boundary layer. The northwest air mass showed an equivalent strength as the southeast air stream, which made pre-dominated southeast air flow a slight bulge at its northwest edge. The slight bulge is corresponding to the PDCB in Fig. 10b and about consistent with the PDCB described in Xue and Martin 2006b, within which the well-mixed moist layer is often half a kilometer or so higher than that to its east. The strong convergence of the two air masses forced a broad uplift of the boundary layer air, with the highest rise located above the bulge, where was also the location of CI-B.

During the convection initially developing along the dryline over CI-B region, a series of dropsondes were deployed from an aircraft between 2110 and 2132 (See Fig. 3c of Murphey et al. 2006). The cross section along the series of dropsondes approximately locates along the line shifting 20 km southward and 30 km westward from that indicated in Fig. 9c. The wind fields, mixing ratio (gray lines), virtual potential temperature ( $\theta_v$ ) and  $\theta_E$  (black lines) along this cross section are compared between the dropsonde observations and the forecast in Fig. 12. Mixing ratio values greater than 7 and 9 g kg<sup>-1</sup> are shaded gray for the observations and the forecast respectively. As the observations, three distinct air masses can be identified in the simulations (Fig. 12c-d). The air mass behind the cold front was relatively cool and moist and persistent northerly flow up to a depth of ~700 hPa. East of the dryline was also relative cool and moist air mass but associated with southerly flow. The dry tongue is shown between the two boundaries as warm, relatively dry, and went with westerly winds. All the three air masses are packed by several isopleths of virtual potential temperature which denote strong stable layers (Fig. 12c). The isopleths of  $\theta_E$  imitating the upward bulge in mixing ratio were also captured in the simulations (Fig. 12d), and the convection first initiated in such region just not far to the northeast at this time (Fig. 11d). The bulge made a well-mixed boundary layer up to ~650 hPa as the observations. Similar moisture bulges associated with deep convergence and updrafts also have been simulated (Ziegler et al. 1997; Xue and Martin 2006a) and observed (Schaefer 1974; Ziegler and Hane 1993; Ziegler and Rasmussen 1998; Ziegler et al. 2007). In addition, The observations show a low-level jet with wind speed greater than 15 m s<sup>-1</sup> locating to the southeast of the dryline (Fig. 12a), while the simulations demonstrate a similar jet structure with stronger winds (20 m s<sup>-1</sup>). The cyclonic secondary circulation left to the jet can enhance the vertical motion there and is believed to have some contributions to the upward bulge near the dryline.

The initial condition along the cross section of CI-C was similar to that of CI-B except the stronger southeast flow (Fig. 11e). By the CI time (Fig. 11f), the enhanced cold front had approached further to southeast with the  $\theta_E$

contours almost vertically distributed within the cold air mass. The stronger southeast air mass was not weakened further as that along the cross section of CI-B, but approximately kept its shape and climbed along the cold front showing an evident uplift there. The boundary layer was also well-mixed up to ~5 km as that for CI-B, while vertical motion showed a wave pattern along and over the cold front. The maximum rise of the 333K  $\theta_E$  contour locating nearly over the surface cold front and above the rear of the uplifted southeast air mass along the cold front, where the first cell of convection C initiated.

Note that the initial cells for CI-A, B, and C first presented at a height of ~6 km MSL, while there were cells also generated ~8 km MSL in CI-C region (Fig. 11b, d, and f). These higher level cells in CI-C region gradually dissipate as the middle level cell developing, and are believed to correspond to the altostratus fractus clouds over south of Kansas as shown in Fig. 4, which are excessively simulated in the model.

### 3) Skew T diagrams of extracted soundings

To reveal the structure and evolution of the boundary layer and the associated convective instability, soundings are extracted from the instantaneous model fields. The locations of nine soundings analyzed here are indicated by labels "Anw", "A", "Ase", "Bnw", "B", "Bse", "Cnw", "C", and "Cse" in Fig. 9a, which are corresponding to the northwest end, center, and southeast end of the cross section lines for CI-A, B, and C, respectively.

Fig. 13 shows the skew  $T$  plots of soundings at location Anw, Ase, Bnw, Bse, Cnw, and Cse extracted at the initial condition time. These soundings show the background structure of the boundary layer behind the cold front and before the dryline, and less changed during the initiation of the three CIs. Anw is located behind the cold front but further near the dry air from the west plateau, the surface air is therefore rather dry with a mixing ratio of 7 g kg<sup>-1</sup> (Fig. 13a). Below 700 hPa exists a conditional unstable layer due to intrusion of the cold front with relative cool and moist northeast air flow under ~3 km MSL. While above 700 hPa is a stable layer about 150 hPa deep and the air within the stable layer is much drier and slightly warmer, reflecting its origin from the west plateau. The dry condition makes the lifting condensation level (LCL) much higher above 600 hPa with small CAPE of 1203 J kg<sup>-1</sup>. Similar patterns can be found in the soundings located at Bnw and Cnw (Fig. 13b-c), except that the stronger intrusion of cold front with stronger north-northeasterly winds induces a temperature inversion at the bottom of the stable layer. Away from the dry region, the surface air becomes moister with  $q_v$  of 9 and 13 g kg<sup>-1</sup> at Bnw and Cnw respectively, the dry condition corresponding to the stable layer also gets weaker with larger  $T_d$ . The LCL decrease to 661 mb and 768 mb while the CAPE increase up to 1515 J kg<sup>-1</sup> and 2441 J kg<sup>-1</sup> at Bnw and

Cnw, while appreciable CIN exists for all the three soundings.

On the southeast side of the dryline and/or cold front, the surface air at Ase and Bse are much moister than that at Asw, Bsw with the dryline locating between them (Fig. 13d-e). While the low-level moist air at Cse has little deference with that at Cnw, which denotes there is a broad region of moist air around the cold front (Fig. 13f). Instead of intrusion of cool and moist air behind the cold front, the low-level south-southwesterly flow under ~800 mb transports relative cool and moist air from the Gulf toward Ase, Bse, and Cse (Fig. 13d-f). Above the low-level moist layer is a stable layer extending up to ~600 mb, which is created by a broad dry air layer between 450 mb and 800 mb driven from west plateau by prevailing southwest winds within this layer. As the air masses at deferent levels moving northeast, the dry air layer mixes with the low-level moist air and weakens its dryness (Fig. 13e-f). The CAPE at Ase is much larger than that at Anw due to dramatic dry-moist differences across the southwestern cold front and dryline. Further northeast across the cold front, the dry-moist differences become smaller and the CAPE at Bse and Cse are slightly larger than that at Bnw and Cnw. The LCLs of the three soundings are much lower than that behind the cold front and slightly decrease from 716 mb, 759 mb, to 780mb through Ase, Bse, and Cse, but considerable CINs associated with the soundings make an impossible condition to initiate convection there.

Fig. 14 shows the soundings located at A from the initial condition time to the time CI-A first initiates. At 1800 (Fig. 14a), A is located between the cold front and the dryline as shown in Fig. 9a. The sounding at this time is similar as that at Anw in Fig. 13a, but with both slightly-larger CAPE and CIN. The low-level dry layer slightly shrinks by 1900 due to the weakening southwest winds below 550 mb (Fig. 14b), and the stable layer has faded away with zero CIN at this time. In the next 40 minutes, the low-level southwest winds are gradually replaced by southeast-southerly flow accompanying the dryline receding toward A. By 1940 (Fig. 14c), a mixed layer has established and deepens up to 600 mb. The CAPE has increased to 2225 J kg<sup>-1</sup> but no saturation is present at this time. Just 10 minutes later (Fig. 14d), the neutrally stable mixed layer has been extended up to ~550 mb, where the profiles of  $T$  and  $T_d$  begin to merge together above the LFC indicating that the saturation condition has been reached to initiate the convection. Note that the LFC for surface parcels is much lower than the saturation point. This is because the parcel  $T$  profile is calculated using the surface air parcels, which is temporarily intruded by the moister flow below 800 mb southeast of the dryline and can't represent the air within the mixed layer. So there should be an up-left shift for the parcel  $T$  profile in Fig. 14d, and the true CAPE for CI-A at 1950 is slightly less than 2756 J kg<sup>-1</sup>.

The sounding located at B where CI-B first initiates is shown in Fig. 15. At 1800 (Fig. 15a), the sounding shows a larger CAPE condition than that at Bnw and

Bse, and there is also a stronger low-level dry layer due to the dry air from the west plateau flowing along the dryline toward B. The mixed layer deepens in the next hours with the surface air keeping its mixing ratio of ~12.5 g kg<sup>-1</sup>. By 2100 (Fig. 15b), the mixed-layer top has increased 850- to 750-hPa level as the potential temperature in the layer rises a few degrees Kelvin. By 2128 (Fig. 15c), the mixed layer continuously extends up to 650-hPa as the low-level dry layer weakens and shifts up to 500-hPa. The CAPE is 3593 J kg<sup>-1</sup> and a small amount of CIN remains at this time. By the time CI-B first initiates (Fig. 15d), the CIN is reduced to zero, the mixed layer becomes well mixed and almost neutrally stable stretching up to ~600-hPa. The LFC is reached freely by the surface parcel at 673 hPa, and saturation has occurred with an evident  $\theta_E$  increase within the 650-450-hPa layer or 3-7 km MSL at this time. This saturation layer matches well the cloud found in the vertical cross section in Fig. 11d with the 10 dBZ reflectivity echo first appearing and centering at ~6 km MSL.

The evolution of sounding located at C is similar as that at B (Fig. 16), except for larger CAPE around 4000 J kg<sup>-1</sup> and much moister surface condition with a mixing ratio of ~15 g kg<sup>-1</sup>. At 1800 (Fig. 16a), the low-level dry layer is slightly weaker than that of sounding B in Fig. 15a as the dry air from the west plateau approaches further northeast there. By 2100 (Fig. 16b), the mixed layer develops from ~850-hPa to ~750-hPa and the CIN is much reduced from -153 to -11 J kg<sup>-1</sup>. The low-level moist layer is well mixed in the next hour, and becomes neutrally stable stretching up to 700-hPa by 2200 (Fig. 16c). Saturation occurs at this time and rapidly spreads up to 500-hPa in the next 10 minutes establishing a ready condition for CI (Fig. 16d). The saturation layer is about between 3 and 6 km MSL at the CI time which is matches the middle level cloud outline in the vertical cross section in Fig. 11f.

Similarly, the deepened moist layer associated with the creation of a deep well-mixed layer clearly contributes to the three CIs. The actual initiations at A, B, and C will be analyzed in detail in Part II, which are resulted from additional forcing by localized features, specifically, by localized surface convergence maxima related to HCRs. Note the secondary moist layer between 300 and 400-hPa or about 9 and 7 km MSL in Fig. 15 and Fig. 16, which corresponding to the upper layer clouds and/or convection in Fig. 11d and Fig. 11f. This layer evolves from a relative moist air with a temperature of about -30 degree Celsius between 400 and 500-hPa at the initial condition time (Fig. 14a, Fig. 15a, and Fig. 16a), and is believed to originate from the southwest relative moist air capping upon the dry air mass from west plateau. The westerly flow between 300 and 400-hPa in sounding A clears away this layer (Fig. 14), while the deep uniform southwesterly winds between 200 and 600-hPa in sounding B and C lift this layer ~100 hPa up (Fig. 15 and Fig. 16). The secondary moist air with low temperature but considerable uplift makes an excessive generation of clouds and/or convections at this layer in

the model (Fig. 11d and Fig. 11f). But as the true convections developing with time, these excessively-generated clouds and/or convection quickly dissipates away (not shown).

## 5. SUMMARY AND CONCLUSION

In this study, the 19 June 2002 convective initiation (CI) case during IHOP\_2002 is simulated in high resolution using a nonhydrostatic mesoscale model, the ARPS, and its data assimilation system, ARPS3DVAR. The initial condition for the simulation assimilates routine as well as special upper-air and surface observations collected during IHOP. The large ( $1000 \times 1000 \text{ km}^2$ ) 1-km grid nested inside in a 3-km grid is able to resolve both important mesoscale environment and smaller convective structures, including many of the boundary layer horizontal convective rolls and individual cells of deep moist convection. Three initiations of convective storms are correctly predicted. CI-A starts in the front-dryline transition zone over southeast Colorado, CI-B forms along the dryline over northwest Kansas, and CI-C locates further north along the cold front over south-central Nebraska. The first focused CI is simulated about 5 km west to the observations with 20 minutes delay, while the timing of CI-B and CI-C are accurate to within 30 min with location errors of 80 and 60 km respectively. The general evolution of the three predicted CIs also verifies well.

The evolution of the vertical structure of the cold front and the dryline shows that CI-A initiates above a strong upsurge of well-mixed neutrally stable and moist layer in the PDCB, CI-B is simulated locating the upward bulge in the isopleths of equivalent potential temperature and mixing ratio as the observations, and CI-C starts over the evident uplift region where strong southeast air mass climbs along the cold front. The low-level moisture convergence bands (MCBs) show different characteristics over the three distinct CI regions. The different CI locations relative to the low-level MCBs suggest that additional lifting from localized forcing associated with HCRs plays a key role in convective initiation. The sounding analyses show that the deepened moist layer associated with the creation of a deep well-mixed layer is clearly essential to the three CIs. The exact processes by which the HCRs interact with the dryline or cold front and how convective cells are initiated will be analyzed in detail in Part II of this study.

Finally, we note that the model simulation presented in this paper is not perfect. The further evolution of the three convective clusters originating from the three CIs is not well organized as the observations. The scattered weak radar echoes observed over Colorado are exaggeratedly predicted. Also over-predicted are the higher level clouds or convective cells (~8 km MSL) near the time of CI-B over northwest Kansas and CI-C over south-central Nebraska. Simulations with different pre-assimilation cycles between 1200 and 1800 will be

demonstrated and compared in Part III of this study to further discuss the sensitivity of these spurious features and their potential reasons.

*Acknowledgement:* Assistance was provided by Dr. Keith Brewster to prepare some initial data. Appreciation goes to Yunheng Wang, Fanyou Kong, Jidong Gao and Guoqing Ge for ARPS/ARPS3DVAR help. A Sun constellation Linux cluster, Ranger, operated by TACC of University of Texas, and a Linux cluster operated by OSCER of University of Oklahoma were used for the simulations.

## REFERENCES

- Brewster, K., 1996: Application of a Bratseth analysis scheme including Doppler radar data. *Preprints, 15th Conf. Wea. Anal. Forecasting*, Norfolk, VA, Amer. Meteor. Soc., 92-95.
- Chou, M.-D., 1990: Parameterizations for the absorption of solar radiation by  $\text{O}_2$  and  $\text{CO}_2$  with application to climate studies. *J. Clim.*, **3**, 209-217.
- , 1992: A solar radiation model for use in climate studies. *J. Atmos. Sci.*, **49**, 762-772.
- Chou, M.-D. and M. J. Suarez, 1994: An efficient thermal infrared radiation parameterization for use in general circulation models. NASA Tech. Memo. 104606, 85 pp.
- Crook, N. A., 1996: Sensitivity of moist convection forced by boundary layer processes to low-level thermodynamic fields. *Mon. Wea. Rev.*, **124**, 1767-1785.
- Fritsch, J. M. and R. E. Carbone, 2004: Improving quantitative precipitation forecasts in the warm season: A USWRP research and development strategy. *Bull. Amer. Meteorol. Soc.*, **85**, 955-965.
- Gao, J., M. Xue, K. Brewster, F. Carr, and K. K. Droegemeier, 2002: New development of a 3DVAR system for a nonhydrostatic NWP model. *Preprint, 15th Conf. Num. Wea. Pred. and 19th Conf. Wea. Anal. Forecasting*, San Antonio, TX, Amer. Meteor. Soc., 339-341.
- Lakshmanan, V., T. Smith, G. Stumpf, and K. Hondl, 2007: The Warning Decision Support System - Integrated Information. *Weather Forecast.*, **22**, 596-612.
- Lin, Y.-L., R. D. Farley, and H. D. Orville, 1983: Bulk parameterization of the snow field in a cloud model. *J. Appl. Meteor.*, **22**, 1065-1092.
- Liu, H. and M. Xue, 2008: Prediction of convective initiation and storm evolution on 12 June 2002 during IHOP\_2002. Part I: Control simulation and sensitivity experiments. *Mon. Wea. Rev.*, **136**, 2261-2282.
- Markowski, P., C. Hannon, and E. Rasmussen, 2006: Observations of convection initiation "failure" from the 12 June 2002 IHOP deployment. *Mon. Wea. Rev.*, **134**, 375-405.
- Murphey, H. V., R. M. Wakimoto, C. Flamant, and D. E. Kingsmill, 2006: Dryline on 19 June 2002 during

- IHOP. Part I: Airborne Doppler and LEANDRE II analyses of the thin line structure and convection initiation. *Mon. Wea. Rev.*, **134**, 406-430.
- Schaefer, J. T., 1974: The life cycle of the dryline. *J. Appl. Meteor.*, **13**, 444-449.
- Stano, G., 2003: A case study of convective initiation on 24 May 2002 during the IHOP field experiment, School of Meteorology, University of Oklahoma, 106 pp.
- Sun, W.-Y. and C.-Z. Chang, 1986: Diffusion model for a convective layer. Part I: Numerical simulation of convective boundary layer. *J. Appl. Meteor.*, **25**, 1445-1453.
- Tong, M. and M. Xue, 2005: Ensemble Kalman filter assimilation of Doppler radar data with a compressible nonhydrostatic model: OSS experiments. *Mon. Wea. Rev.*, **133**, 1789-1807.
- Weckwerth, T. M. and D. B. Parsons, 2006: A review of convection initiation and motivation for IHOP\_2002. *Mon. Wea. Rev.*, **134**, 5-22.
- Weckwerth, T. M., D. B. Parsons, S. E. Koch, J. A. Moore, M. A. LeMone, B. B. Demoz, C. Flamant, B. Geerts, J. Wang, and W. F. Feltz, 2004: An overview of the international H<sub>2</sub>O project (IHOP\_2002) and some preliminary highlights. *Bull. Amer. Meteorol. Soc.*, **85**, 253-277.
- Wilson, J. W. and R. D. Roberts, 2006: Summary of convective storm initiation and evolution during IHOP: Observational and modeling perspective. *Mon. Wea. Rev.*, **134**, 23-47.
- Xue, M. and W. J. Martin, 2006a: A high-resolution modeling study of the 24 May 2002 dryline case during IHOP. Part I: Numerical simulation and general evolution of the dryline and convection. *Mon. Wea. Rev.*, **134**, 149-171.
- , 2006b: A high-resolution modeling study of the 24 May 2002 dryline case during IHOP. Part II: Horizontal convective rolls and convective initiation. *Mon. Wea. Rev.*, **134**, 172-191.
- Xue, M., J. Zong, and K. K. Droegemeier, 1996: Parameterization of PBL turbulence in a multi-scale non-hydrostatic model. *Preprint, 11th AMS Conf. Num. Wea. Pred.*, Norfolk, VA, Amer. Meteor. Soc., 363-365.
- Xue, M., K. K. Droegemeier, and V. Wong, 2000: The Advanced Regional Prediction System (ARPS) – A multi-scale nonhydrostatic atmospheric simulation and prediction model. Part I: Model dynamics and verification. *Meteorol. Atmos. Phys.*, **75**, 161-193.
- Xue, M., D. Wang, J. Gao, K. Brewster, and K. K. Droegemeier, 2003: The Advanced Regional Prediction System (ARPS), storm-scale numerical weather prediction and data assimilation. *Meteorol. Atmos. Phys.*, **82**, 139-170.
- Xue, M., K. K. Droegemeier, V. Wong, A. Shapiro, K. Brewster, F. Carr, D. Weber, Y. Liu, and D. Wang, 2001: The Advanced Regional Prediction System (ARPS) - A multi-scale nonhydrostatic atmospheric simulation and prediction tool. Part II: Model physics and applications. *Meteorol. Atmos. Phys.*, **76**, 143-165.
- Ziegler, C. L. and C. E. Hane, 1993: An observational study of the dryline. *Mon. Wea. Rev.*, **121**, 1134-1151.
- Ziegler, C. L. and E. N. Rasmussen, 1998: The initiation of moist convection at the dryline: Forecasting issues from a case study perspective. *Weather Forecast.*, **13**, 1106-1131.
- Ziegler, C. L., T. J. Lee, and R. A. Pielke, 1997: Convective initiation at the dryline: A modeling study. *Mon. Wea. Rev.*, **125**, 1001-1026.
- Ziegler, C. L., E. N. Rasmussen, M. S. Buban, Y. P. Richardson, L. J. Miller, and R. M. Rabin, 2007: The "triple point" on 24 May 2002 during IHOP. Part II: Ground-radar and in-situ boundary layer analysis of cumulus development and convection initiation. *Mon. Wea. Rev.*, **135**, 2443-2472.

Table 1. List of the abbreviations of the observation networks used in this study and some of their characteristics.

Type of dataset	Abbreviation	Description	Temporal resolution	Special or standard	Number of stations
Upper-air datasets	RAOB	NWS radiosonde network	3 hour	data at 1200 are standard, others are considered special	30 at 1200 missing at 1500 11 at 1800
	WPDN	Wind Profiler Demonstration Network	1 hour	standard	30
	COMP <sup>*</sup>	Special composite dataset composed of many upper-air observing networks	1 hour	special	1
	MDCRS	NWS Meteorological Data Collection and Reporting System aircraft observations	1 hour	special	varies
Surface datasets	SAO	Surface observing network composed of the ASOS and the FAA surface observing network	1 hour	standard	about 286
	COAG	Colorado Agricultural Meteorological Network	1 hour	special	29
	OKMESO	OK Mesonet	1 hour	special	About 138
	SWKS	Southwest Kansas Mesonet	1 hour	special	8
	GWMD	Kansas groundwater Management District #5 Network	1 hour	special	10
	WTX	West Texas Mesonet	1 hour	special	30
	ARM	Atmospheric Radiation Measurement Southern Great Plains Surface Meteorological Data	1 hour	special	11

\* A description on the individual networks included in the composite can be found in Stano (2003).

Table 2. List of analyzed observations and the horizontal and vertical filter length scales used by each pass of the ARPS3DVAR analysis

Pass No.	Analyzed observations	horizontal influence radius in km	vertical influence radius in grid points
1	RAOB, WPDN, COMP, and MDCRS	320	4
2	RAOB, WPDN, COMP, MDCRS and SAO	160	4
3	SAO, COAG, OKMESO, SWKS, WTX, GWMD and ARM	80	2
4	SAO, COAG, OKMESO, SWKS, WTX, GWMD and ARM	50	2
5	COAG, OKMESO, SWKS, WTX, GWMD and ARM	30	2

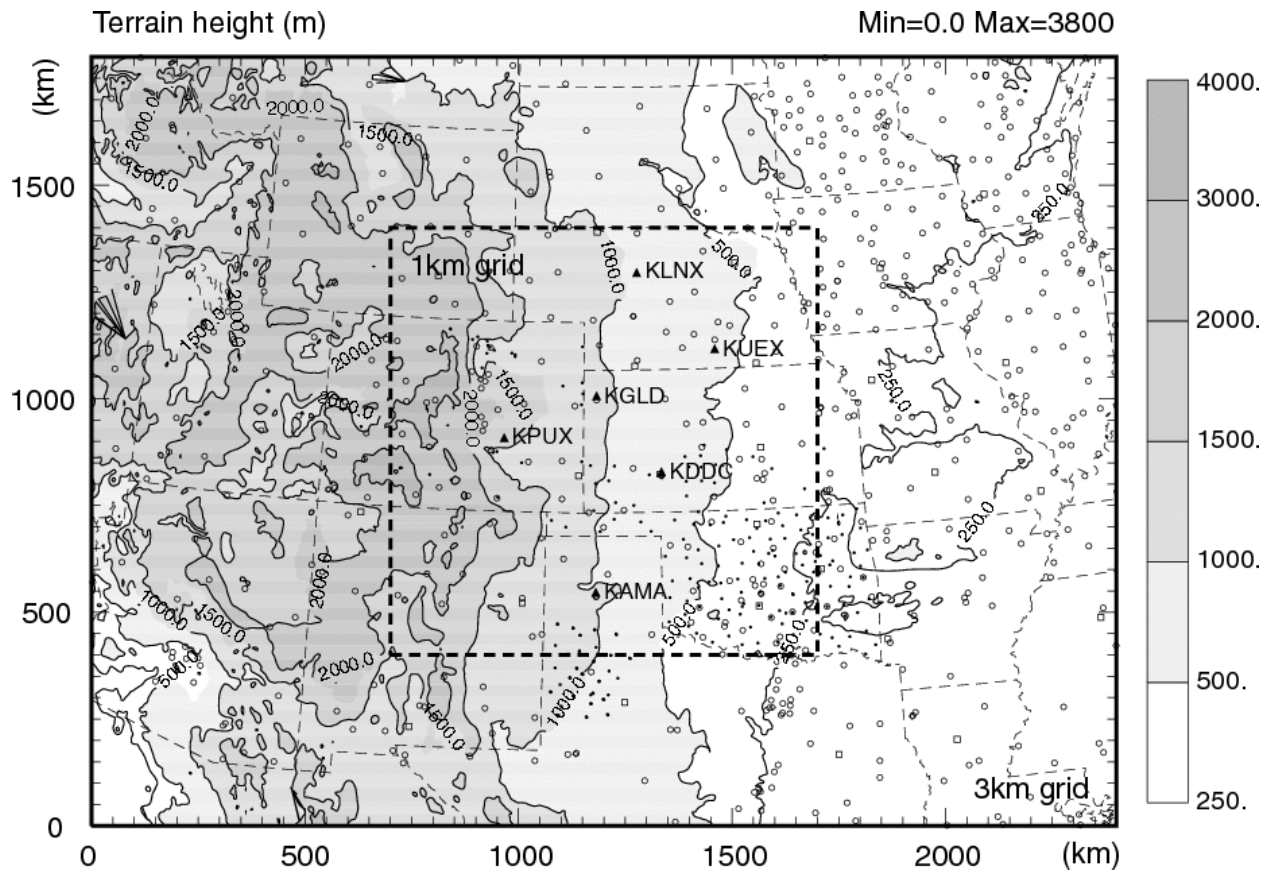


Fig. 1. The 3-km model domain with terrain elevation shaded. The nested 1-km domain is indicated by the dashed rectangular box. The filled upward triangles indicate the radar locations of KLNX, KUEX, KGLD, KPUX, KDDC, and KAMA respectively; the stations of the Oklahoma Mesonet, the West Texas Mesonet, the southwest Kansas mesonet, the Kansas groundwater management district #5 network, and the Colorado agricultural meteorological network are marked by small dots; the stations from ASOS and the FAA SAO are marked by circles; the stations from the NWS radiosonde network are marked by squares; and the stations from the NOAA wind profiler network are marked by diamonds. Also shown are state boundaries.

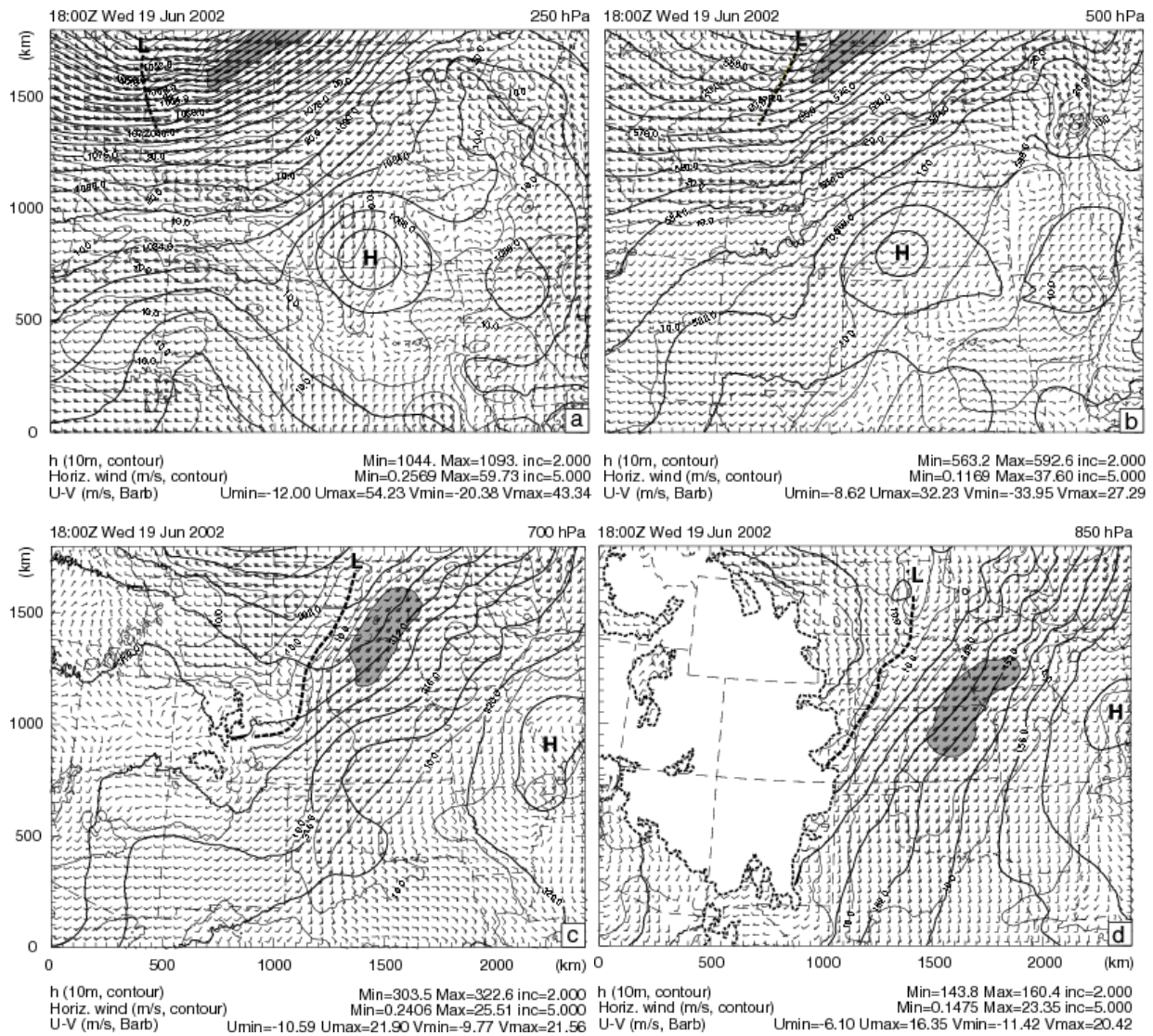


Fig. 2. Geopotential height (thick black contours, 10m), wind speed (thin black contours,  $\text{ms}^{-1}$ ), and wind barbs (one full bard =  $5 \text{ ms}^{-1}$ ) at 1800 UTC 19 June 2002, at (a) 250-, (b) 500-, (c) 700-, and 850-hPa levels. Bold dashed lines indicate the locations of trough lines, and areas with wind speed exceeding  $55 \text{ ms}^{-1}$  at 250 hPa,  $35 \text{ ms}^{-1}$  at 500 hPa,  $20 \text{ ms}^{-1}$  at 700 hPa, and  $20 \text{ ms}^{-1}$  at 850 hPa are shaded gray. Thin dashed lines in (c) and (d) demonstrate the 700 hPa and 850 hPa contours at surface, respectively.

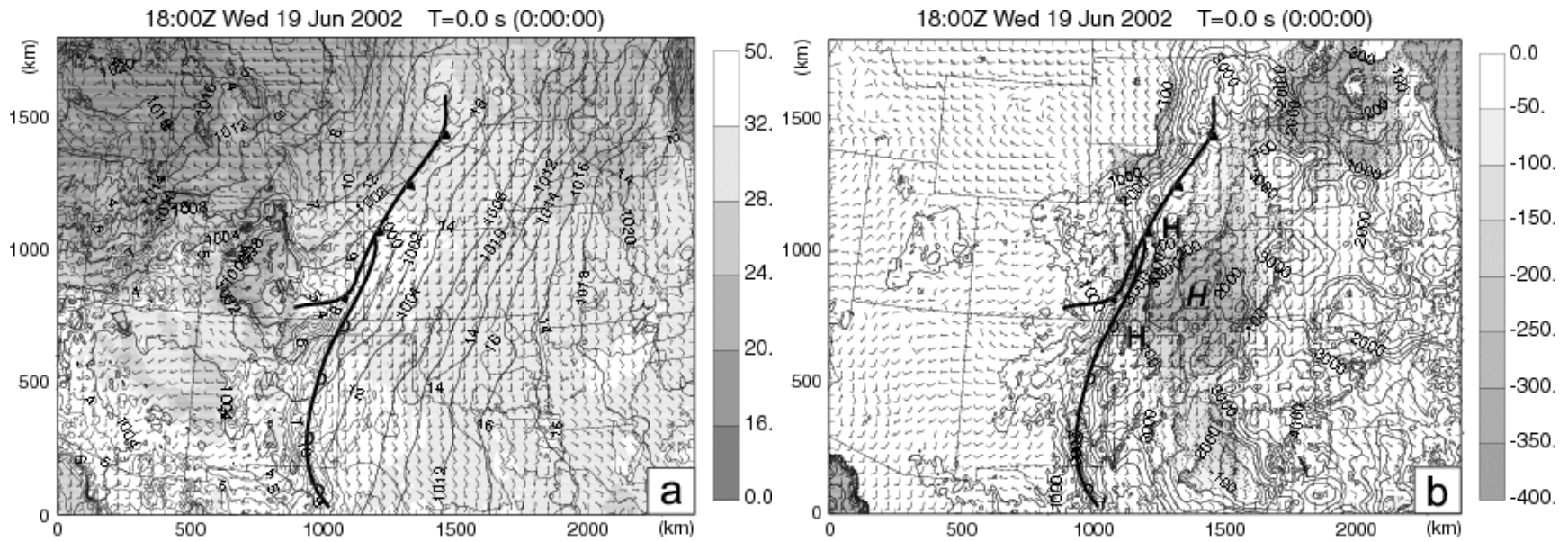


Fig. 3. The surface fields analysis at 1800 UTC 24 May 2002: (a) Mean sea level pressure (thick black contours, hPa), temperature (shaded, °C), water vapor mixing ratio (thin black contours, g kg<sup>-1</sup>), and the wind field (full barb represents 5 m s<sup>-1</sup>, half barb 2.5 m s<sup>-1</sup>); (b) wind fields, CAPE (contours, J kg<sup>-1</sup>, with maximum centers near triple point marked by **H**), and CIN (dashed contours with gray shading, J kg<sup>-1</sup>, with maximum centers near triple point marked by **H**). Cold front and dryline are marked by standard symbols.

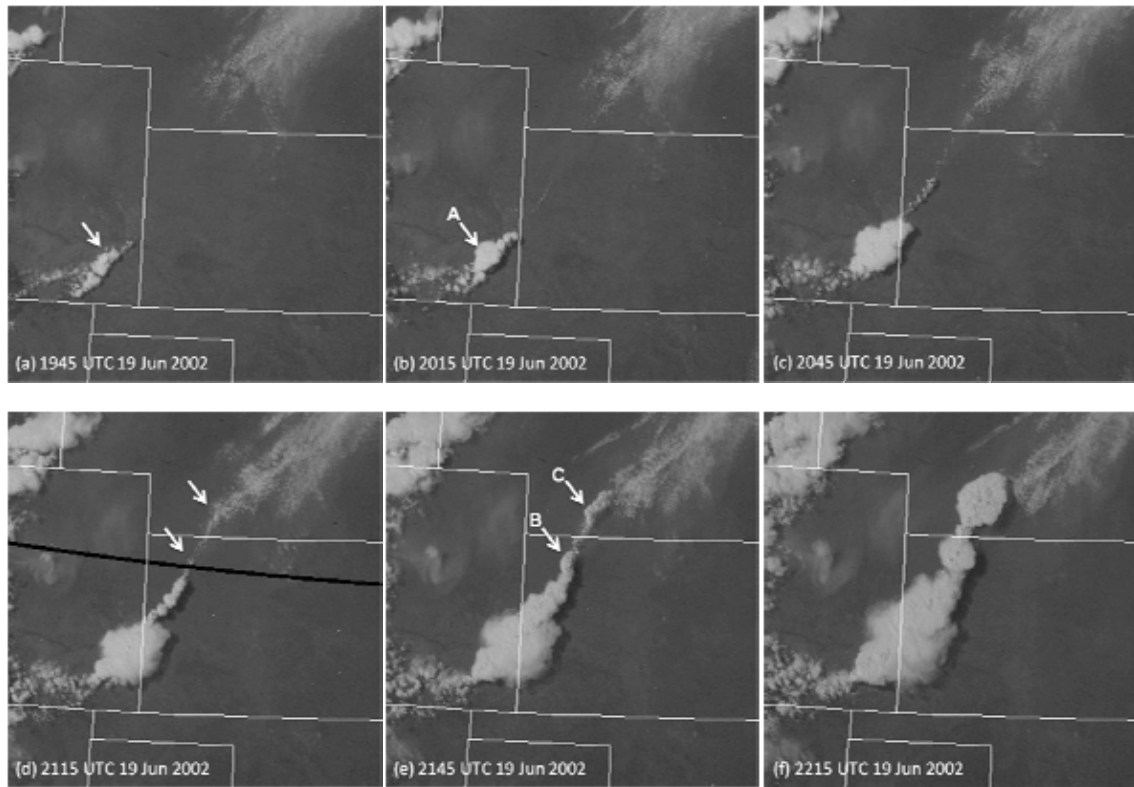


Fig. 4. GOES visible satellite images taken at (a) 1945, (b) 2015, (c) 2045, (d) 2115, (e) 2145, and (f) 2215 UTC 19 June 2002.

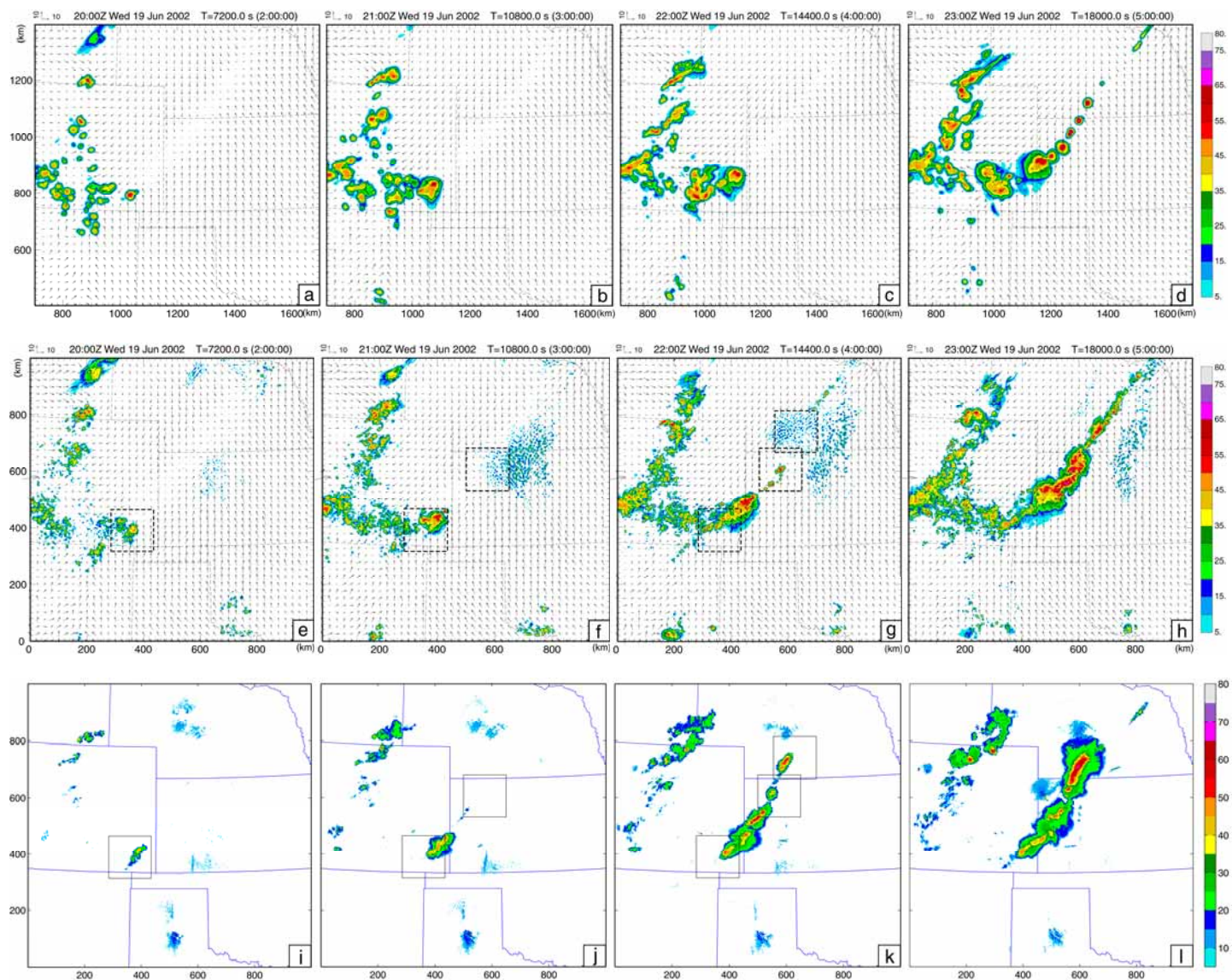


Fig. 5. ARPS 3-km forecast composite reflectivity (color shaded) of control data assimilation experiment together with surface wind vectors at (a) 2000, (b) 2100, (c) 2200, and (d) 2300 UTC 19 June 2002. The plots of (e)-(h) and (i)-(l) are the same as (a)-(d) but for the nested 1-km forecast and the observed composite reflectivity fields, respectively.

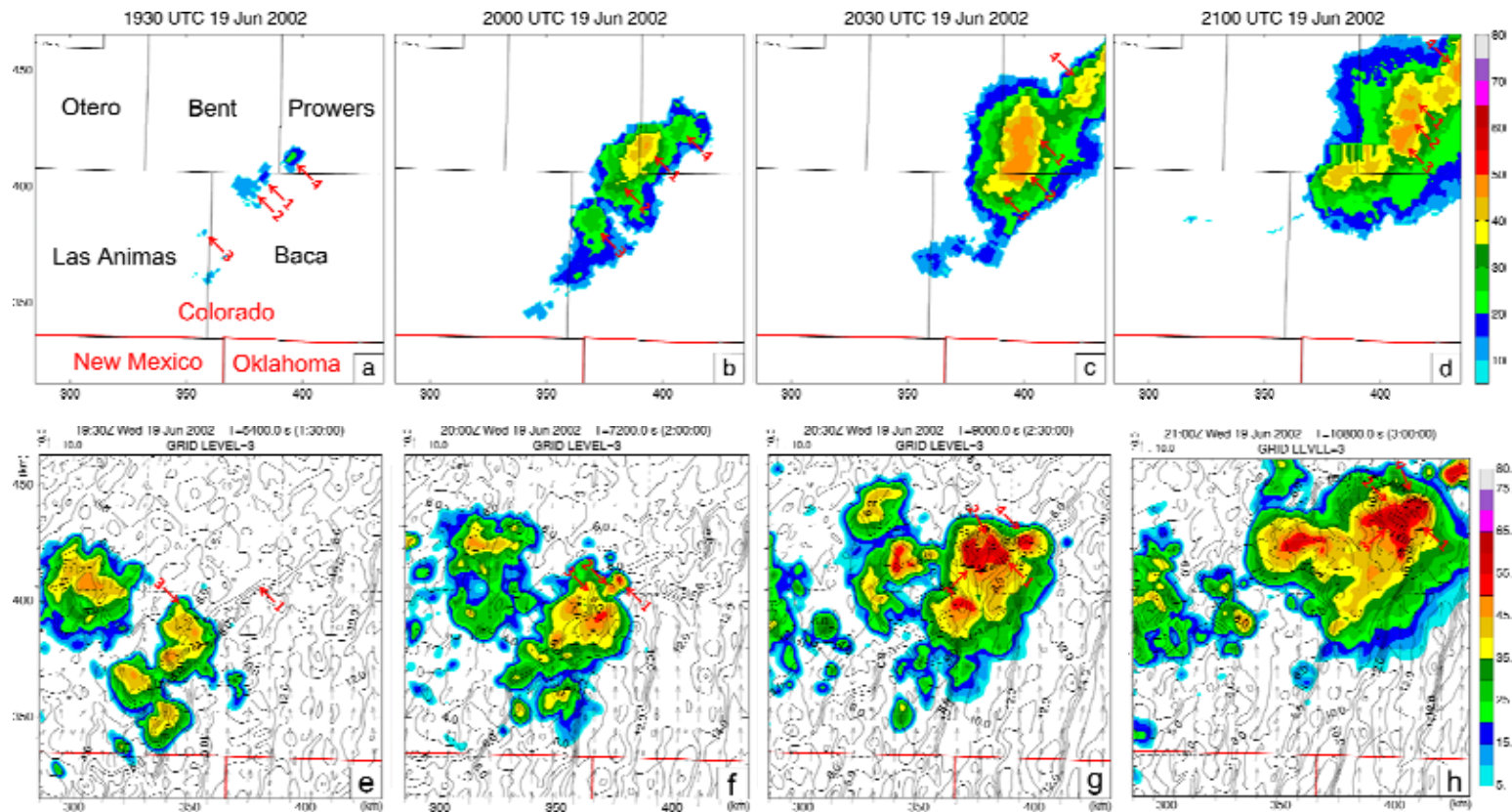


Fig. 6. Evolution of CI-A. Observed composite reflectivity fields (color shaded) at (a) 1930, (b) 2000, (c) 2030, and (d) 2100 UTC 19 June 2002. The plots (e)-(h) are correspond to the times of (a)-(d), but for ARPS 1-km forecast composite reflectivity of the control data assimilation, together with wind vectors and water vapor mixing ratio (contours) near surface (about 30m AGL). Four convective cells are identified with numbers. The counties and states are labeled in (a). The domain corresponds to the square box over southeastern Colorado in Fig. 5e.

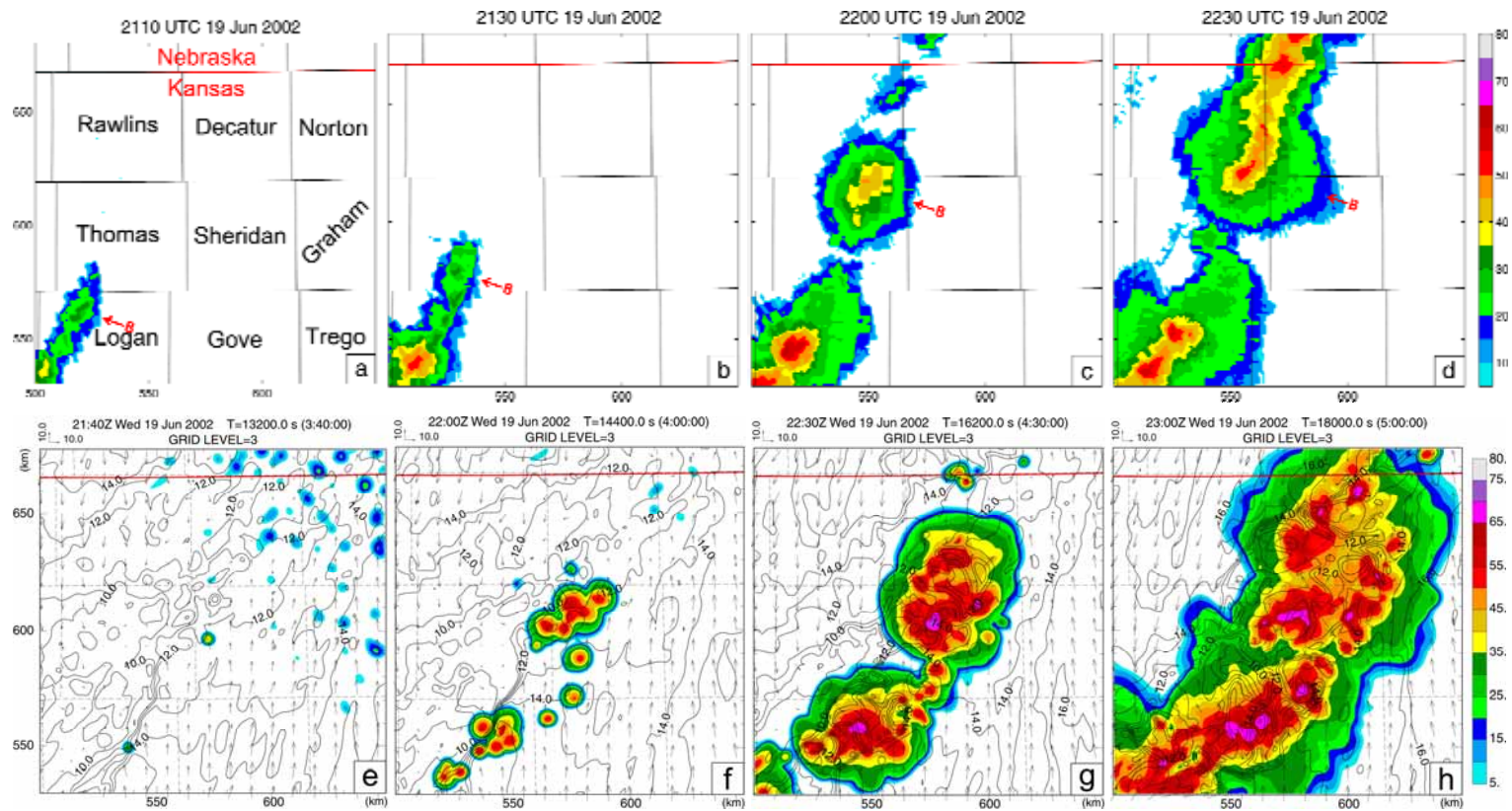


Fig. 7. The same fields as in Fig. 6, but for CI-B with observation fields (a) 2115, (b) 2230, (c) 2200, and (d) 2230 UTC, and forecast fields at (e) 2145, (f) 2200, (g) 2030, and (h) 2300 UTC 19 June 2002, respectively. The observed convection B is marked with arrows in (a)-(d). The counties and states are labeled in (a). The domain corresponds to the square box over northwest Kansas in Fig. 5f.

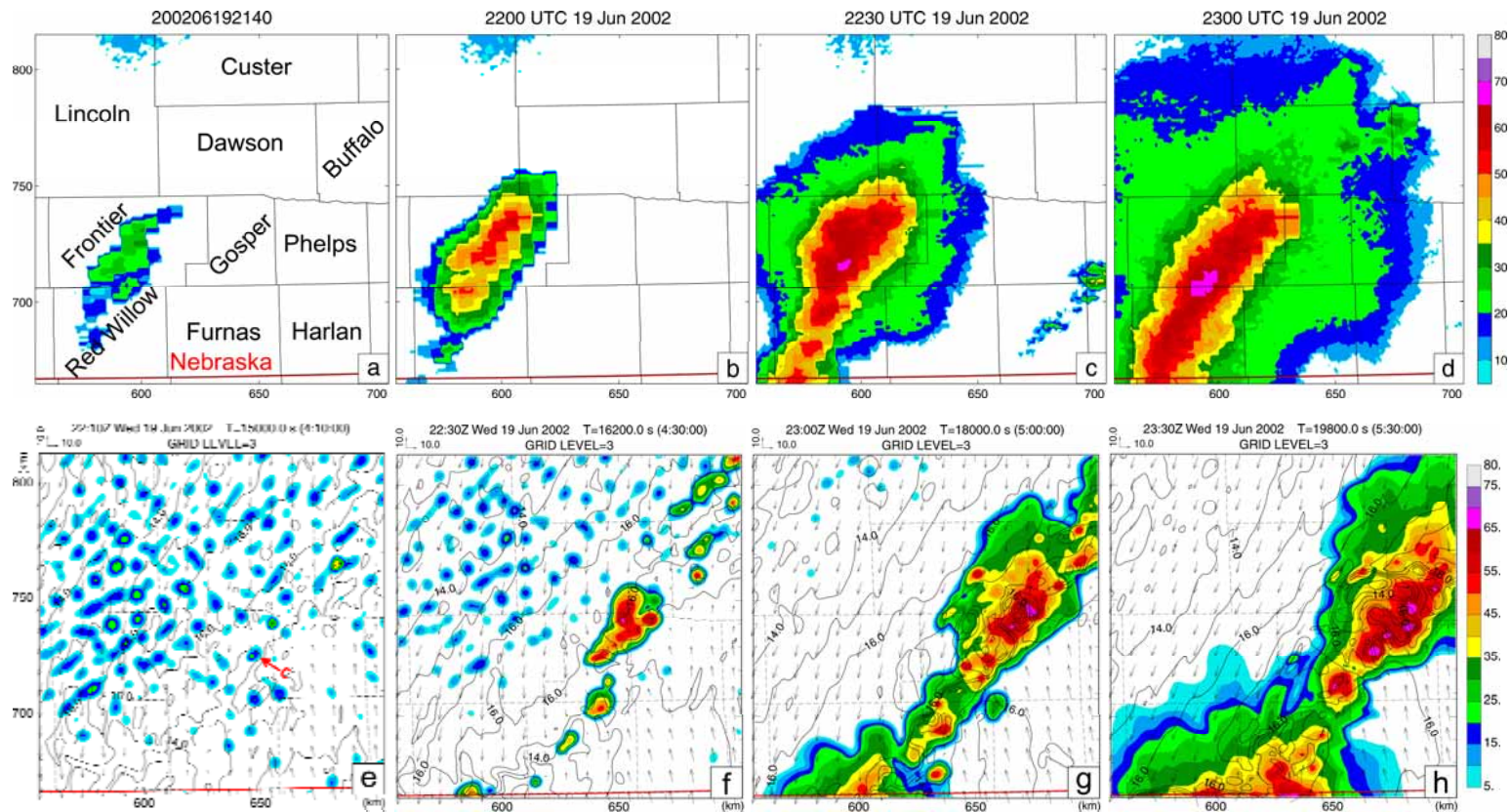


Fig. 8. The same fields as in Fig. 6, but for CI-C with the observation fields at (a) 2140, (b) 2200, (c) 2230, and (d) 2300 UTC, and the forecast fields at (e) 2210, (f) 2230, (g) 2300, and (h) 2330 UTC 19 June 2002, respectively. The simulated initiation cell C is tagged in (e). The counties and states are labeled in (a). The domain corresponds to the square box over south-central Nebraska in Fig. 5g.

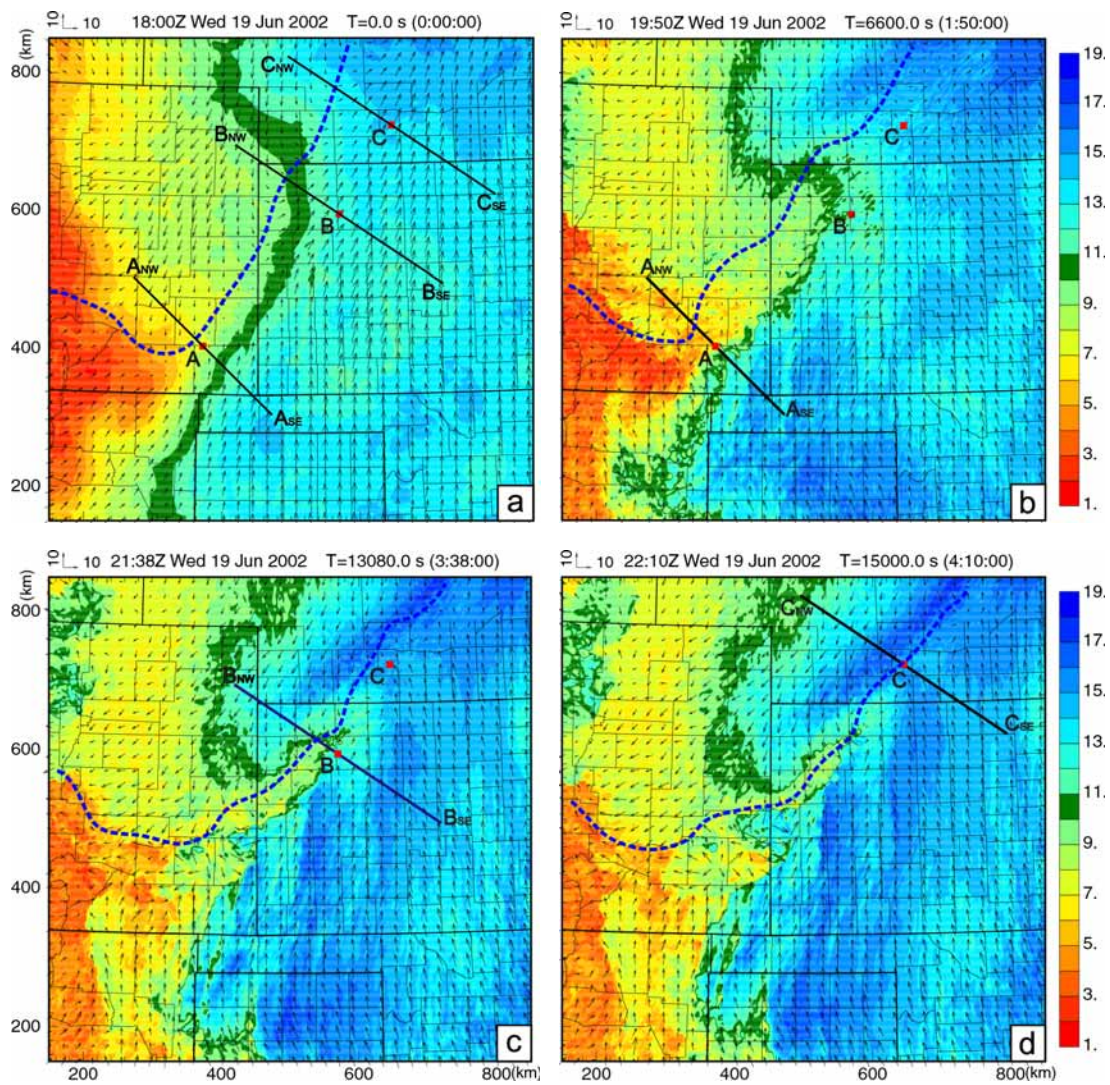


Fig. 9. Surface  $q_v$  (shaded,  $\text{g kg}^{-1}$ ) and wind fields (vector unit shown in the plots,  $\text{m s}^{-1}$ ) at (a) the initial condition time, (b) 1950, (c) 2138, and (d) 2210 UTC June 2002. The times of (b)-(d) correspond to the minutes that 10~20-dBZ composite reflectivity contours first appear for storm cells of the three CIs. The labels A, B, and C mark the locations where the CI-A, CI-B, and CI-C first initiates. The dashed lines denote surface cold front, and the 10-11  $\text{g kg}^{-1}$   $q_v$  fields (darker green shaded) before the cold front outline the dryline. Thick black lines indicate locations of vertical cross sections to be shown in Fig. 11.

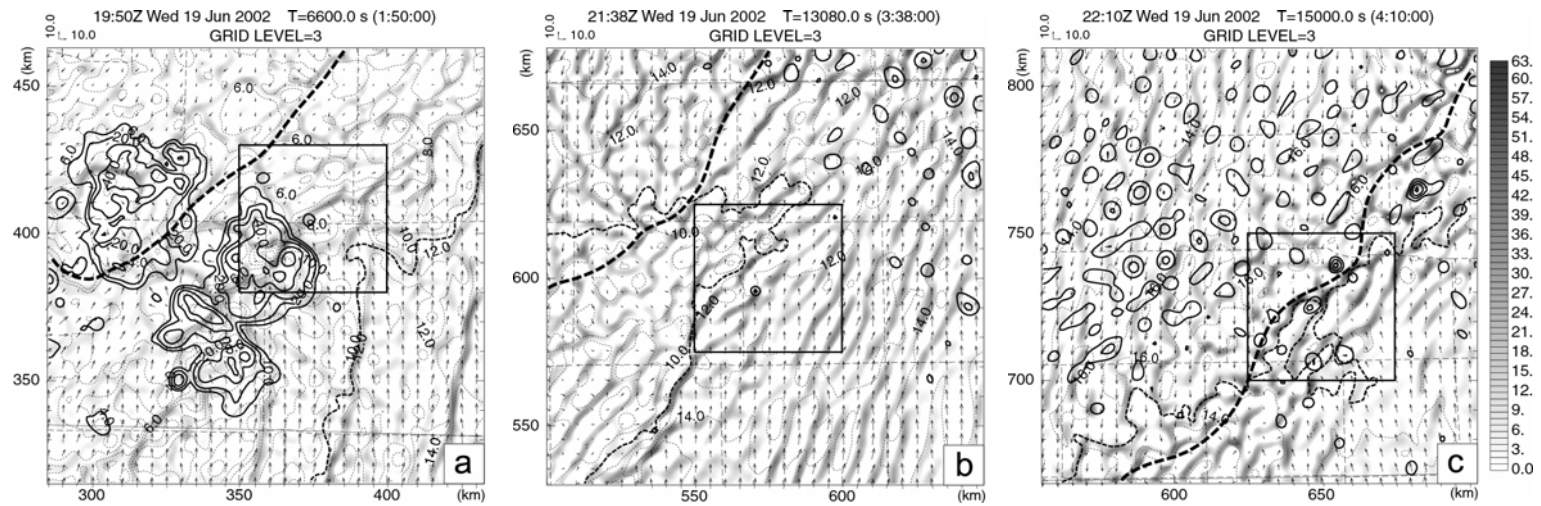


Fig. 10. Model-simulated near-surface (about 30m AGL) moisture convergence field (gray shading, values amplified by a factor of 1000, and only positive values shown), the horizontal wind vectors (vector unit shown in the plots,  $\text{m s}^{-1}$ ), the  $q_v$  field in thin-dashed contours, and the composite reflectivity in full thick contours for (a) CI-A at 1950, (b) CI-B at 2138, and CI-C at 2210 UTC June 2002. The times correspond to that of Fig. 9b-d. The bold thick-dashed lines denote the cold front, the thick-dashed  $11 \text{ g kg}^{-1}$   $q_v$  lines represent the dryline or dry air boundaries. An enlarged view of the boxed regions in (a)-(c) is shown in Fig. 1-3 of Part II.

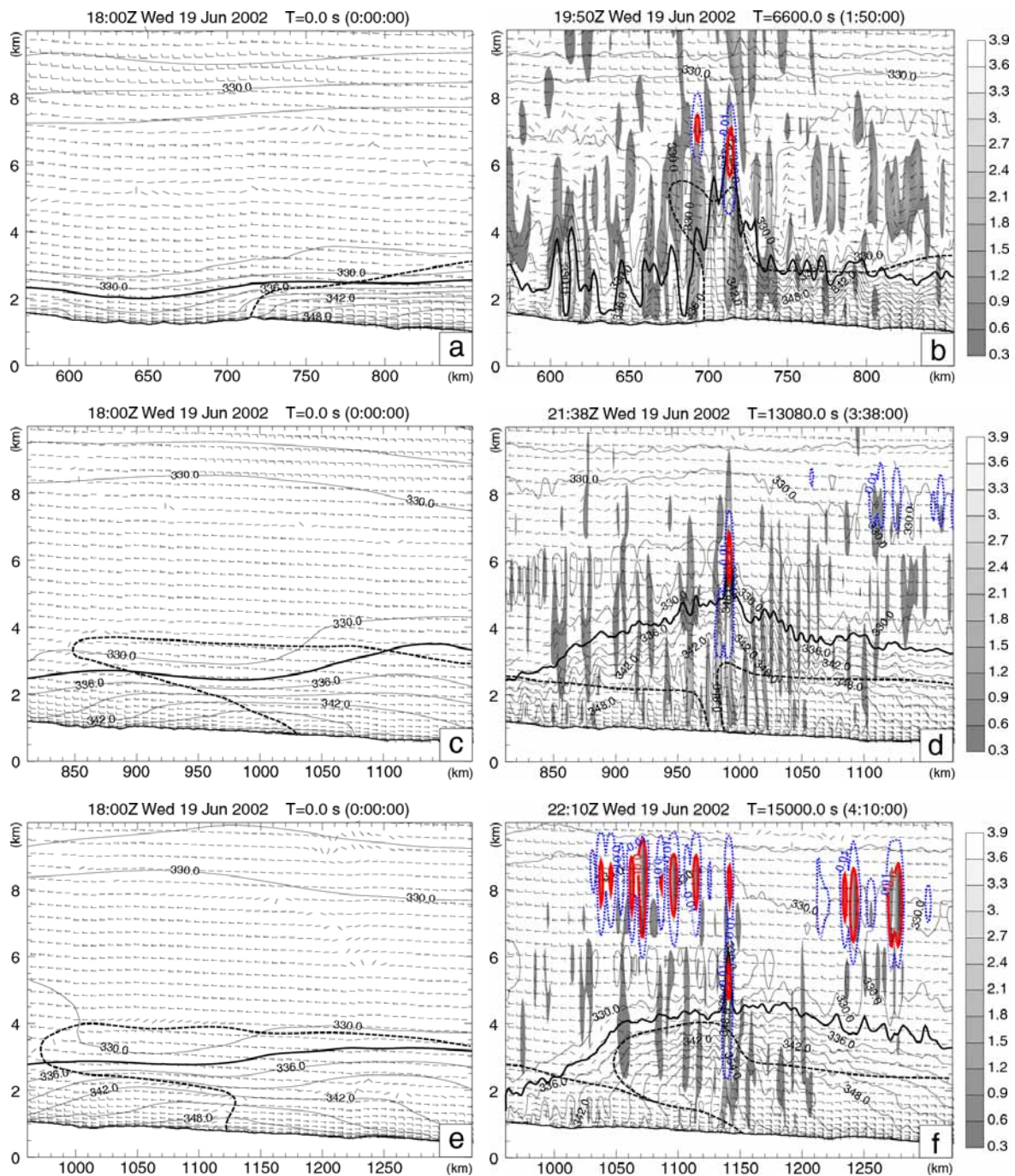


Fig. 11. Northwest-southeast cross sections of equivalent potential temperature (contours, K), gray-shaded vertical velocity (only positive values are show,  $m s^{-1}$ ), wind fields (barbs), the  $0.01 g kg^{-1}$  total condensed water/ice outlining the clouds (bold dashed contours), and the 10 dBZ reflectivity (bold solid contours), for (a)-(b), (c)-(d), and (e)-(f) through the black thick lines in Fig. 9b, c, and d respectively. The plots of (a), (c), and (e) are at the initial condition time, while (b), (d), and (f) are at the corresponding times of Fig. 9b, c, and d. The 333 K equivalent potential temperature is thickly contoured. The low-level air masses along the cross sections are outlined with thick-dashed lines.

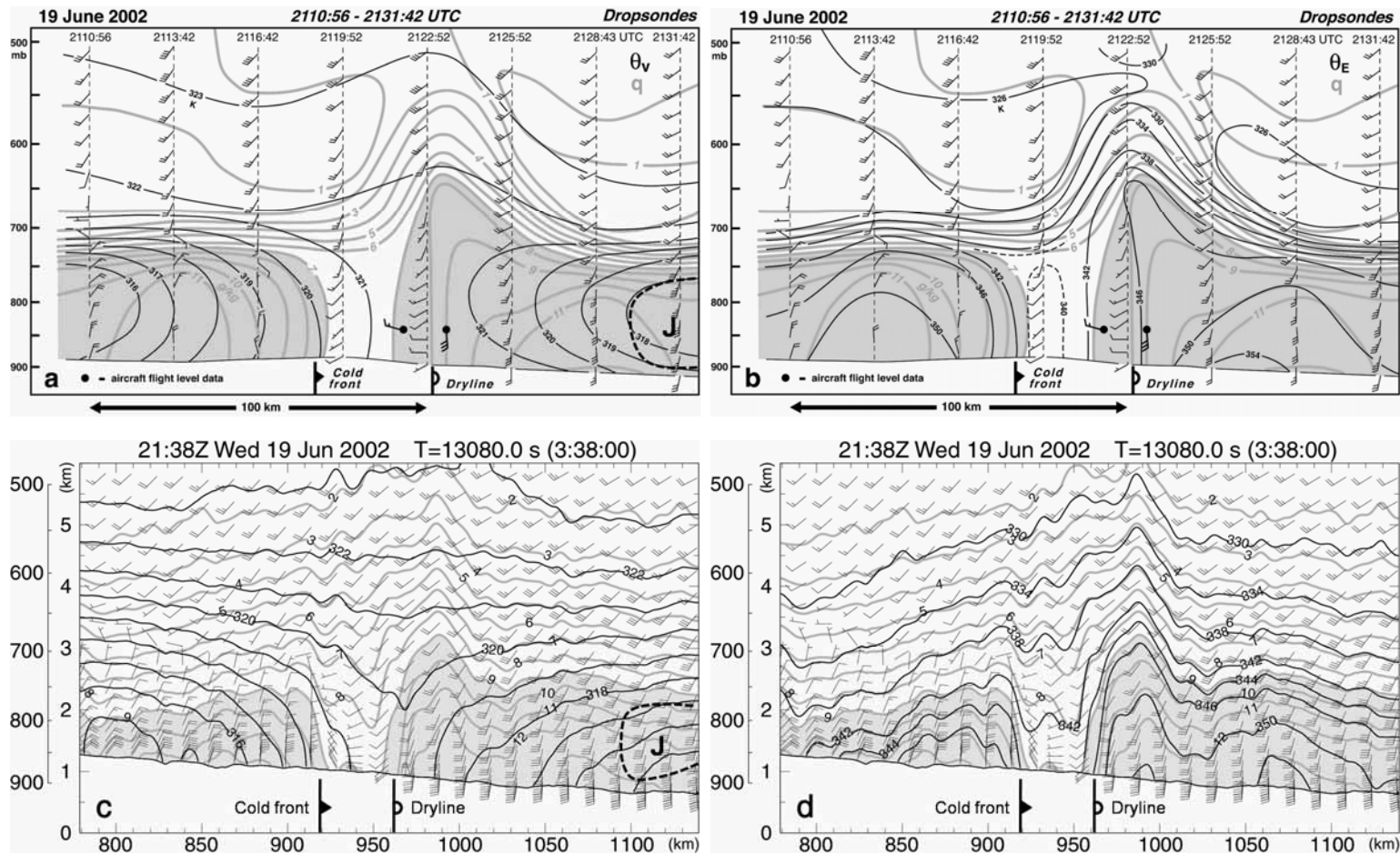


Fig. 12. Observed and simulated northwest-southeast cross section of winds, mixing ratio (gray lines) for CI-B. Observations based on a series of dropsondes deployed from an aircraft with (a) virtual potential temperature and (b) equivalent potential temperature (From Murphey et al. 2006); The plots (c) and (d) are the same as (a) and (b), but for highly-smoothed model output at 2138 UTC, along the line shifting 20 km southward and 30 km westward from that indicated in Fig. 9c, which approximately represents the line along the series of dropsondes.

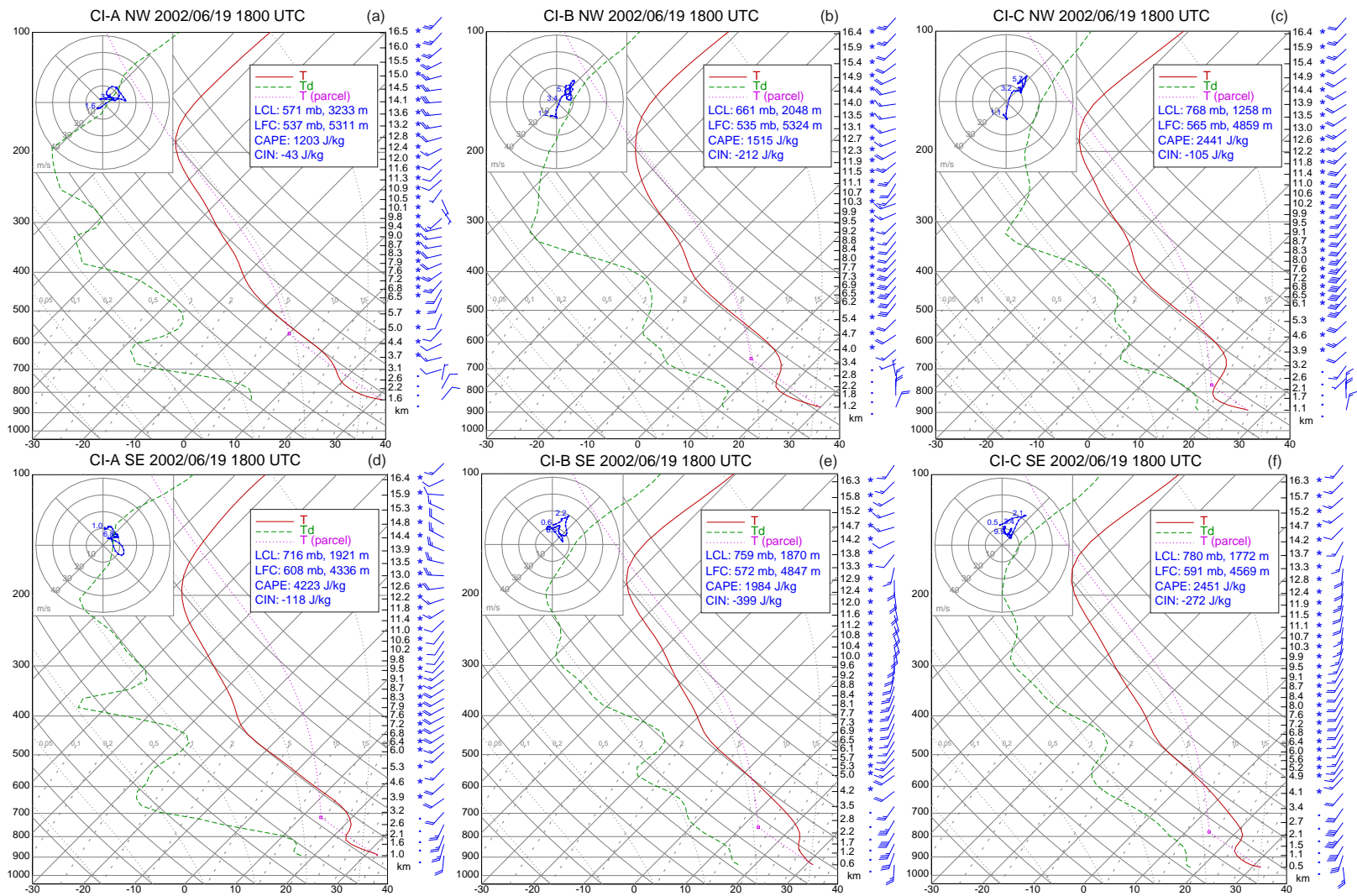


Fig. 13. Skew  $T$  plots of soundings at 1800 UTC extracted from model forecasts at the locations labeled in Fig. 9, for (a) at “Anw”, (b) at “Bnw”, (c) at “Cnw”, (d) at “Ase”, (e) at “Bse”, and (f) at “Cse”.

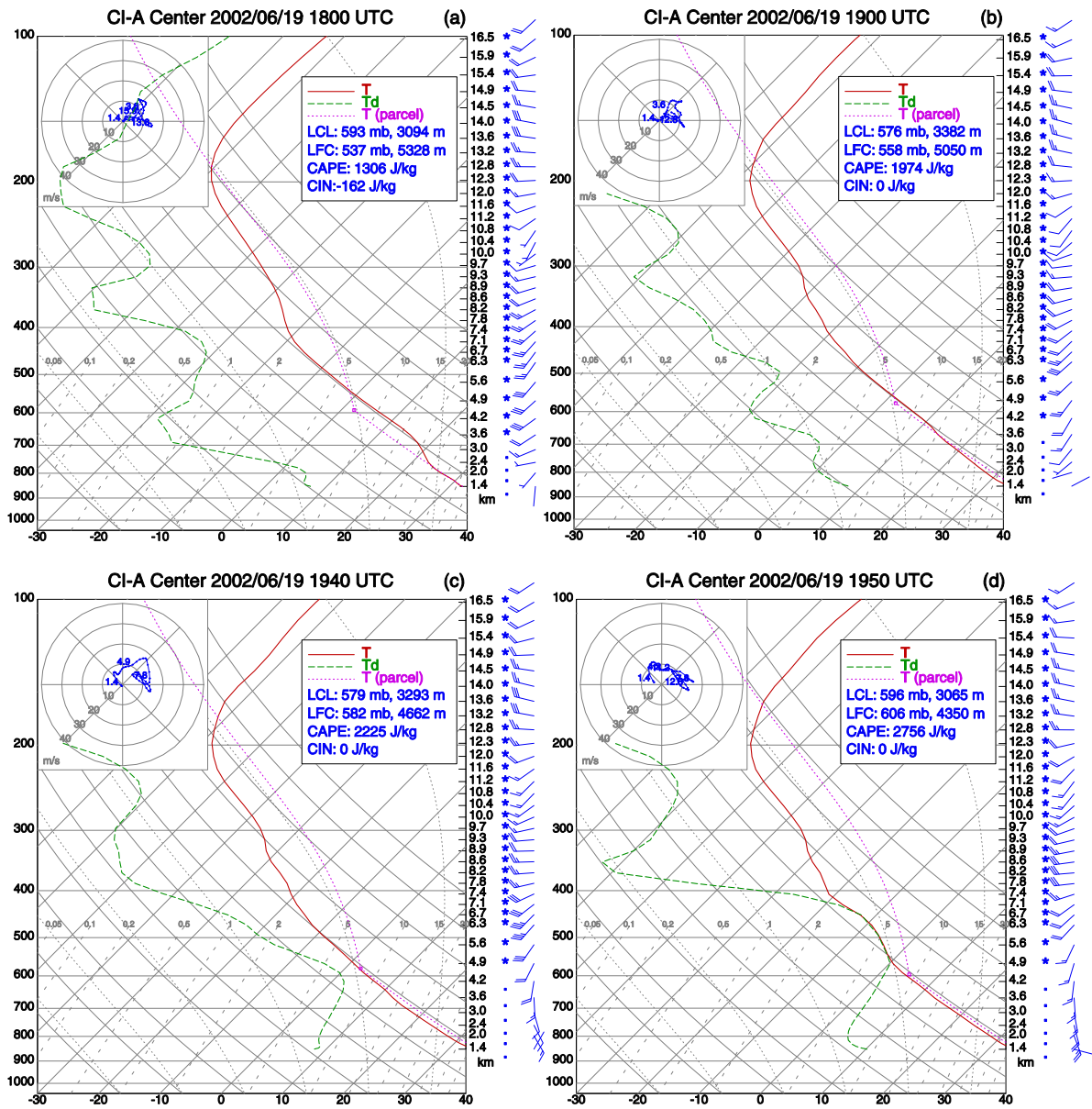


Fig. 14. Skew T plots of soundings extracted from model forecasts at CI-A location labeled "A" in Fig. 9b, at 1800, 1900, 1940, and 1950 UTC.

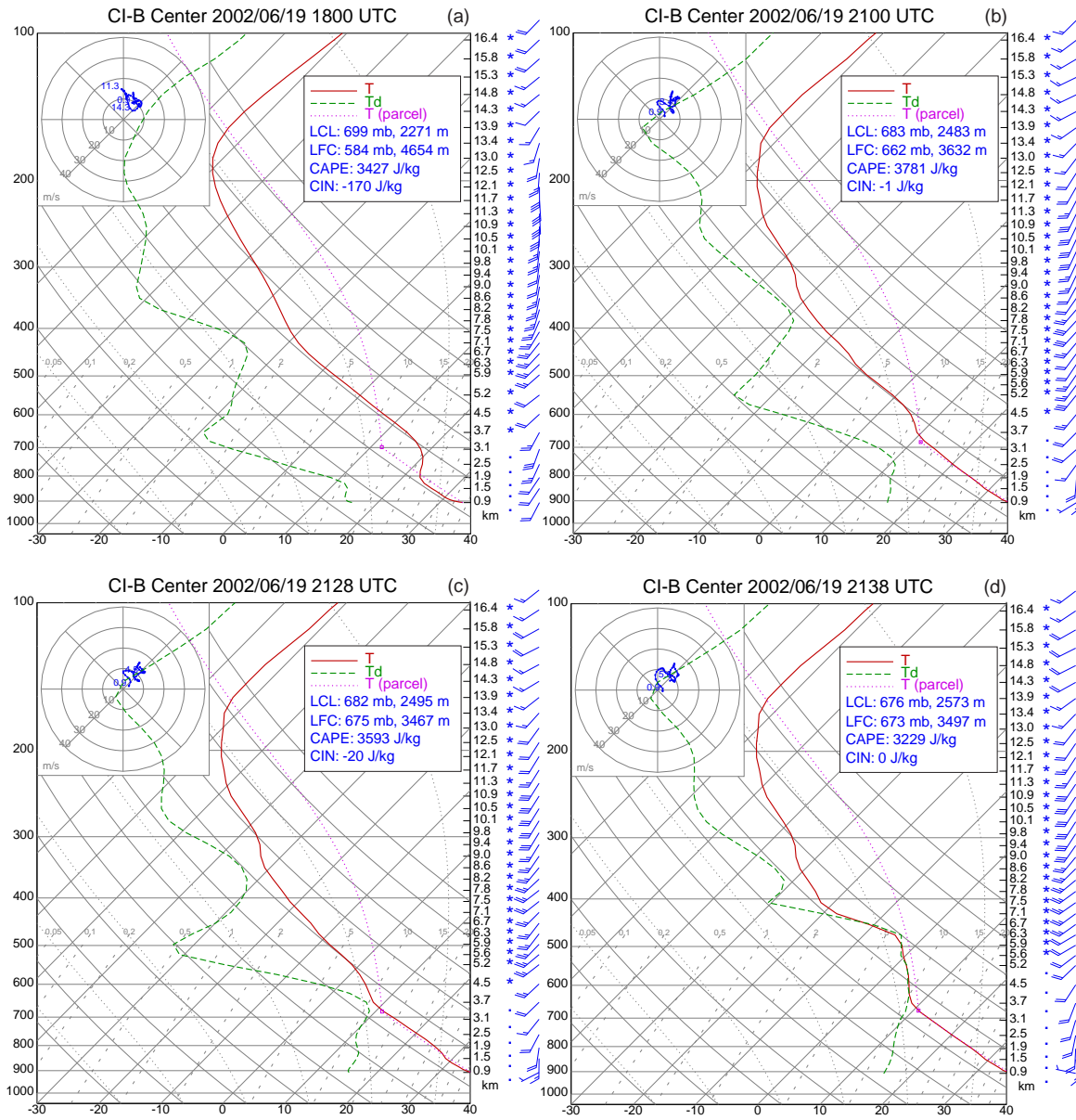


Fig. 15. Skew T plots of soundings extracted from model forecasts at CI-B location labeled "B" in Fig. 9c, at 1800, 2100, 2128, and 2138 UTC.

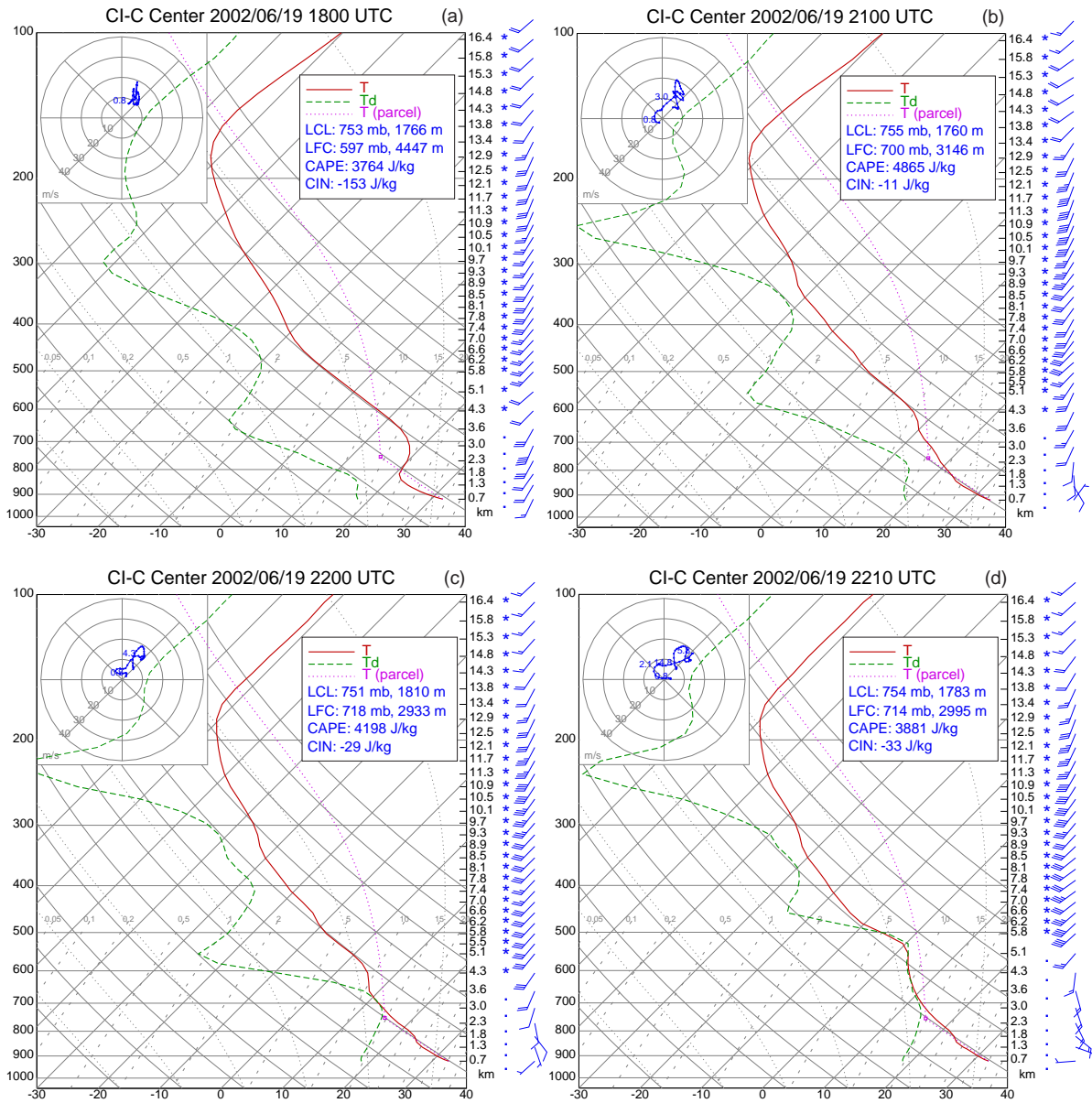


Fig. 16. Skew T plots of soundings extracted from model forecasts at CI-C location labeled "C" in Fig. 9d, at 1800, 2100, 2200, and 2210 UTC.